Available online at https://link.springer.com/journal/42241
http://www.jhydrodynamics.com
Journal of Hydrodynamics, 2021, 33(3): 421-447
https://doi.org/10.1007/s42241-021-0052-6

URANS simulations for a free-running container ship: Part 1. Turning-circle *

Dong-Hwan Kim[1, 2], Yugo Sanada[1], Sungtek Park[1], Hamid Sadat-Hosseini[3], Frederick Stern[1]
1. *IIHR-Hydroscience and Engineering, The University of Iowa, Iowa City, USA*
2. *Costal Development and Ocean Energy Research Center, Korea Institute of Ocean Science and Technology, Busan, Korea*
3. *Mechanical Engineering, University of North Texas, Denton, USA*

(Received May 3, 2021, Revised May 8, 2021, Accepted May 10, 2021, Published online July 5, 2021)

Abstract: The incompressible unsteady Reynolds-averaged Navier-Stokes (URANS) simulations are performed for a free-running container ship in maneuvering conditions: the starboard and portside turning circle simulations with 35° rudder deflection. The validation variables include trajectory, motions, and propeller performances, and the prediction shows acceptable agreements against the experimental data. During the steady-state part of the turning, the inertial forces balancing the local forces are reported to quantitatively assess the centrifugal force which appears from the force equilibrium between the rudder, propeller, and the bare-hull. The study on the local flow focuses on finding the correlations between the propeller inflow and the propeller performance to investigate the differences in propeller performances during the portside and starboard turning. The preliminary simulations, performed with the grid triplet, comprise propeller open-water, resistance, and self-propulsion simulations, from which the validation studies and the studies for the local force and the local flow are fulfilled and applied for the main simulations. Both propeller and rudder are fully discretized and controlled, mimicking the experiment. Level-set, overset approach and Mentor's SST model are employed for the free-surface capturing, large motion prediction, and turbulence closure.

Key words: Turning-circle, unsteady Reynolds-averaged Navier-Stokes (URANS), KRISO Container Ship (KCS), CFDShip-IOWA

Introduction

The validation of the computational fluid dynamics (CFD) simulations for the maneuvering test conditions have been providing the reliable chronological flow fields, global variables, trajectory data, yet the complete understanding for the motion mechanism or the propeller performance is still veiled by the complexity or the sensitivity of the governing equations. The characteristics of the maneuvering condition that are distinguished from the self-propulsion condition are as follows: (1) 2-D trajectory, (2) unsteady motion/flow during the short amount of transitional stage that affects the entire trajectory, (3) six degree of freedom (6DOF) motions which shows strong coupling for surge, sway, yaw rate and drift angle, (4) 3-D behavior of the local flow field including the vortex-induced from the bare-hull and the boundary layers of the bare-hull that converges differently at the stern and results in different propeller inflow pattern on account of the ship motion, (5) fluid exerted lateral force and resistance allocated for changing the direction of the ship and are the cause of the speed loss, and (6) increase of rudder contribution on the yaw moment, and thereby, the increased demand of accurate prediction for the rudder force.

To simplify the test condition, the current study focuses on the steady-state turning condition where the ship experiences the circular motion clearly. The same grid resolution is assessed for both turning and self-propulsion simulation. The error values for motions and propeller performance are compared to confirm the discrepancy of prediction accuracy. The global forces and moment are localized: the forces and moment of bare-hull, rudder stock, moving rudder, and propeller are found to check the contribution of each part during the force equilibrium, and the centrifugal force in steady-state turning is estimated to confirm the amount of the counterforce quantitatively. Since the bare-hull is exposed to the 3-D flow extensively, compared to the other appendages, the local force of the bare-hull undergoes further localization and is distributed to longitudinal stations. The characteristics of the propeller inflow and the propeller blade forces that show a strong correlation to

* **Biography:** Dong-Hwan Kim (1988-), Male, Ph. D.,
E-mail: dhk@kiost.ac.kr
Corresponding author: Frederick Stern,
E-mail: frederick-stern@uiowa.edu

the propeller inflow is compared with the self-propulsion simulation, and the difference of the characteristics between the portside turning and the starboard turning is stated. The study results fulfilled from the current paper is confined to explaining the phenomena at the lower complex condition. However, the results are expected to provide meaningful information for future investigations. The free-running experimental data are provided from Sanada et al.[1]

The previous studies that assess maneuvering conditions utilizing CFD are focused on evaluating the trajectory and the global variables of the ship and the propeller: Sadat-Hosseini et al.[2] compared the discretized propeller and the potential theory-based body-force propeller for the free-running KRISO Very Large Crude Carrier 2 (KVLCC2) unsteady Reynolds-averaged Navier-Stoke (URANS) simulations. The test condition included Froude number (Fr) 0.142 starboard 35° turning circle and both starboard 10/10 and 20/20 zigzag. The side force of the body-force propeller and the International Maritime Organization (IMO) criteria were evaluated. Sadat-Hosseini and Stern[3] simulated the 5415M turning test and zigzag using URANS and axisymmetric body-force propeller to improve the system-based method. Carrica et al.[4] used an axisymmetric body-force propeller for 5415M. The test condition included +35 turning and 20/20 zigzag for Fr = 0.250 and 0.410. Mofidi and Carrica[5] simulated 10/10 and 15/1 zigzag for the KRISO Container Ship (KCS) equipped with the discretized actual propeller and the discretized rudder. The delayed-DES was used as a turbulence model. Muscari et al.[6] used URANS with the body-force propeller for the twin-propeller frigate maneuvering test. Zou et al.[7] used the in-house URANS code for the maneuvering ship neglecting motions and free-surface. Kaidi et al.[8] used a body force propeller with FLUENT in the bank channel. Wang and Wan[9] simulated the free-running KRISO Very Large Crude Carrier 1 (KVLCC1) equipped with the discretized propeller and the moving rudder using the OpenFOAM-based in-house code. The model scale was 1/110, and the targeted Froude number was 0.142. The code used $k-\omega$ SST turbulence model using wall function, and the overset grid technique was applied. The solver simulated the reversing propeller using a PI controller and provided the trajectory, ship speeds, global/local force, and moments and local flow to assess the stopping maneuverability.

1. Model description

Figure 1 presents the KCS model studied in the current paper. The ship is a conceptual model resembling the modern 3600 TEU class container ship. Various experimental and numerical research have been performed utilizing the KCS model since early 2000 for the in-depth investigation on the flow characteristics and the motion responses of a mid-speed ranged commercial ship. The ship is single screwed and employed with a horn-type rudder and KP505 propeller. As the tests become diverse, a wave breaker is mounted at the front deck of KCS to prevent the overflow during the bow plunging. Table 1 reports the main dimensions and the characteristics of bare-hull (BH), rudder (RUD), and propeller (PROP). The following subsections provide detailed explanations for each part.

1.1 *Bare-hull*

The scaling factor (λs) decided by the Froude number similarity is 85.19, which derives the 2.7 m length between the perpendicular ($L_{PP} = L$) model for the current study. The other main dimensions of the bare-hull, such as breadth (B), depth (D), and draft (T) are directly calculated from the scaled bare-hull's surface grid, which is manually generated based on a database, and show very close scaled values to the design value. The wetted area (A_W) and the longitudinal center of gravity (LCG) of the bare-hull are computed by performing the hydrostatic computation at even keel, zero speed condition.

During the hydrostatic computation, the LCG is arbitrarily moved along the longitudinal axis until the trim moment becomes lower than the threshold. The final value of LCG for the given numerical model is $0.4848L$, having less than 0.1% difference error from the design value, and the amount of error is considered satisfactory. Getting correct wetted area and LCG considering only hydrostatic force ensures that the overlapped surface grid resolves the database accurately, not being prone to simulation accuracy. The grid overlap is permitted with the overset technique, and more explanation on the approach will be presented in the computational method section. The

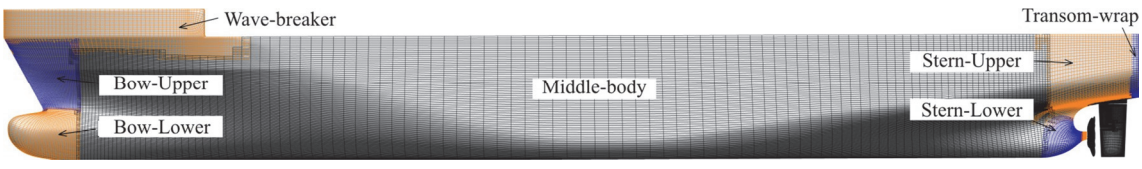

Fig. 1 (Color online) Grid composition of the bare-hull assembly ($g3$)

Table 1 Main particulars and characteristics

Part	Symbol	Full scale	Current
BH	λ_s	1	85.19
	L_{PP} [m]	230	2.7
	B [m]	32.2	0.378
	D [m]	19	0.223
	T/L	0.04696	0.04696
	A_W/L^2	0.1802	0.1805[3, 5]
	LCG/L	0.4852	0.4848[3, 4]
	KG/L	-	0.0622[1]
	$T_z/(L\cdot U^{-1})$	-	0.463[2]
	$T_\theta/(L\cdot U^{-1})$	-	0.450[(2)]
	$T_\phi/(L\cdot U^{-1})$	-	1.946[2]
	k_{xx}/B	0.4	0.43[2]
	k_{yy}/L	0.25	0.25[1]
	k_{zz}/L	0.25	0.25[1]
RUD	r_{rub} [°·s^{-1}]	2.32	21.5[1]
	r_x/L	1.00	1.00
PROP	N_P	5	5
	D_P [m]	7.9	0.093
	P_x/L	-	0.9825[1]
	P_z/L	-	–0.02913[1]

Note: [1]Experiment data is used, [2]Estimated from decay simulation, [3]Estimated from hydrostatic simulation, [4]Distance from the aft perpendicular [5]0.1842 for the fully assembled grid.

vertical center of gravity (KG) presented as $0.0622L$ is the vertical distance from the keel, and the value is measured from the experiment. Natural heave, pitch, and roll periods (T_z, T_θ, T_ϕ), estimated from Part 2, are 0.463, 0.450 and 1.946 when scaled. The natural periods are affected by the grid and the radius of gyration inputs as well as the accuracy of the code. The axial radius of gyration (k_{xx}) is the estimated value computed along with roll frequency during the roll decay simulation, the measured $k_{xx} = 0.39B$ by swing tests in the air is used as an input, and the value is adjusted iteratively by running a couple of roll decay simulations. Measured values are directly used for the y and z-axis radius of gyrations (k_{yy}, k_{zz}).

1.2 *Rudder*

The rudder is divided into two parts: rudder stock (RS) and moving rudder (MR). The moving rudder has single freedom along the rudder axis and can rotate to 35° in each portside and starboard side. Rudder angle (δ) is positive when the trailing edge moves to the starboard. The longitudinal location of the rudder axis (r_x) is the same as the location of the aft perpendicular (A.P.): one characteristic length away from the forward perpendicular (F.P.). The rudder stock is fixed to the bare-hull and does not have any motion with respect to the ship. The rate of rudder angle (r_{rud}) is set to 21.5 °/s, mimicking the experiment. However, the value does not significantly affect the steady-state or quasi-steady-state simulations where the moving rudder is not displaced dynamically. In Part 2, where the unsteady behavior is expected due to wave excitement, matching the rate of rudder angle with the experiment is crucial for accurate validation.

1.3 *Propeller*

The number of blades (N_P) of the current propeller is five, and the diameter (D_P) is 0.093 m. The longitudinal propeller center (p_x) and the vertical propeller center (p_z) are away from the forward perpendicular and waterline by $0.9825L$ and $0.02913L$, respectively. The rotation direction is clockwise when the ship is seen from the rear. The propeller hub cap is not resolved in the simulations and is designed as flat instead, while the experimental model is still equipped with the hub cap. The absence of the hub cap is expected to induce a chaotic hub vortex towards the rudder. However, the amount of its cause is not estimated in the current study.

2. Test conditions and validation variables

The simulation cases are divided into preliminary simulations and maneuvering simulations. Table 2 presents the summary of simulation cases. The preliminary simulations cover (1) propeller open-water simulation (POT), (2) resistance simulation (RES), and (3) self-propulsion simulation (SP). The validation studies on the global variables and the studies for the local flow and local force are carried on before the maneuvering simulations for a generalized assessment of the current setup. As main simulations, the turning circle simulations (TC) with ±35° rudder deflection are performed. During the assessment of the maneuvering simulations, the same approaches performed from the self-propulsion simulation are applied to ship in the steady-state turning. The comprehensive terminology for comprising the simulations except for the propeller open-water test is the calm water simulations.

2.1 *Propeller open-water simulation*

The propeller open-water simulation aims to assess the current propeller grid through validation study and extract the propeller open-water curves to estimate the self-propulsion factors in self-propulsion maneuvering simulations. The range of targeted advance ratio covers 0.1 to 0.9. The propeller rotational speed (n) is fixed to 20 revolutions per second (rps), and the magnitude of incoming uniform flow is varied to derive each advance ratio. To simulate the propeller rotation, the constantly increasing roll is prescribed for the propeller, and the time step is fixed to 7.22×10^{-5} s, which gives out near 0.5° rotation per iteration. The whole domain rotates with the propeller at the same rotational speed to avoid executing the overset process at every iteration. The experiment also fixed the propeller rotation speed and changed the towing speed. The validation variables are thrust/torque coefficients (K_T, K_Q) and the propeller open-water efficiency (η_0).

2.2 *Resistance simulation*

In resistance simulation, the bare-hull grid is assessed through the validation of resistance components and motions. The rudder is equipped, however, its effect is found insignificant. The Froude number is 0.26, which is identical to the conditions targeted from the self-propulsion and maneuvering simulations, and the time step is fixed to 5.25×10^{-3} s. Validation variables include sinkage (σ), trim (τ), total resistance (C_T), and its components, skin frictional resistance coefficient, and residuary resistance coefficient (C_F and C_R) measured/calculated at the carriage frame. The predicted total resistance value accounts for estimating the hull efficiency during the self-propulsion and maneuvering simulations. As a local flow study, the axial velocity distribution inside the propeller disk is averaged (ω_D), and the grid convergence is confirmed.

Table 2 Simulation test matrix

Test	DOF	J / Fr	Re^* (10^6)	δ	Grid
POT	1	0.10 0.20 0.40 0.60 0.70 0.75 0.80 0.90	0.50 1.00 2.01 3.01 3.51 3.77 4.02 4.52	-	$g1$, $g2$, $g3$
RES	2	0.26	3.61	0	$g1$, $g2$, $g3$
SP	6	0.26	3.61	0, PI	$g1$, $g2$, $g3$
TC	6	0.26	3.61	±35	$g2$, $g3$

Note: *Based on ship characteristic length

2.3 *Self-propulsion simulation*

A fully assembled grid is used in the self-propulsion simulation. The global variables for both ship and propeller and self-propulsion factors are validated. The ship is in free-running condition, and both propeller and rudder are controlled actively. At the beginning of the simulation, the ship is towed at target Froude number for a short amount of time with the prescribed surge motion and the initial propeller rotation speed is fixed to experimental value to shorten the computational time required to put the ship at the target Froude number with the corresponding propeller rotational speed. As both constraints are taken off, the boundary layers of the ship and the local flows near the propeller and the rudder are still not fully developed. However, the surge velocity and the propeller rotational speed are much closer to their final values than starting from the zero speed for both ship and propeller. Furthermore, the ship does not experience abrupt acceleration/motion. The released ship eventually reaches a quasi-steady-state with the predicted steady propeller rotational speed and the biased rudder angle. The biased rudder angle is called the neutral rudder angle (δ_N) in this paper. The validation variable includes motions, propeller rotational speed, thrust/torque coefficients, self-propulsion factors, neutral rudder angle, and the local flow value ω_D. An additional simulation is carried out with the fixed rudder to confirm the effect of the neutral rudder angle. The pressure distribution on the rudder surface, the angle of attacks at the leading edge of the rudder, and the local forces are compared with the results fulfilled

with the active rudder condition to confirm the effect of the neutral rudder angle. As a final step, to infer the source of the neutral rudder angle, the propeller inflow, propeller wake, and a single propeller blades' forces are extracted, and descriptions of their correlation are stated. The proportional gain (K_P) of 80 and integral gain (K_I) of 120 are used for both propeller rotational speed and the rudder. However, gains are ineffective for the quasi-steady-state outcomes. The time step for the self-propulsion simulation is 4.2×10^{-4} s, which is required for rotating the propeller at 1.43° per iteration.

2.4 *Maneuvering simulation*

The turning-circle simulations start from the quasi-steady-state self-propulsion simulation conducted with the active rudder. Therefore, the rudder starts its deflection from the neutral rudder angle. The propeller rotational speed is no longer predicted and is fixed with the final quasi-steady-state value, which is averaged over enough time duration during the self-propulsion stage. The rudder angle linearly changes from the neutral rudder angle to the target angle with the rudder rate shown in Table 1. Assessment on the fine grid is refrained for maneuvering simulation due to the high computational cost. Still, the performance of the medium grid is confirmed. Validation variables are composed with IMO criteria, motions, drift angle (β), thrust/torque coefficients, and self-propulsion factors similar to self-propulsion simulation. The simplified equations of motion are derived for the quasi-steady-state turning condition. The inertial force is calculated using the predicted ship speed and the yaw rate to investigate the equilibrium of the equation of motion. Also, the local forces and moments are extracted to have insight into force equilibrium within the body-fixed frame and the contribution of the rudder. The propeller inflow is extracted and correlated with the propeller blade's force to explain the difference between propeller performance during the starboard and portside turning. The result is also compared against the self-propulsion simulation result. The longitudinal distributions of the hydrodynamic forces and the moment are compared with the self-propulsion results. The time step for maneuvering simulations is identical to the value used in the self-propulsion simulation, which derives a very close propeller rotation angle per iteration.

3. Computational methods

3.1 *CFDShip-IOWA V4.5*[11]

The code, developed from IIHR–Hydroscience and Engineering, apply the finite difference method for the standard URANS

$$\frac{\partial \overline{u}_i}{\partial t}+u_j\frac{\partial \overline{u}_i}{\partial x_j}=-\frac{1}{\rho}\frac{\partial \overline{p}}{\partial x_j}+\frac{\partial}{\partial x_j}\left[(\nu+\nu_t)\frac{\partial \overline{u}_i}{\partial x_i}\right]+g_j \qquad (1)$$

where each pressure term and gravitational acceleration are contributory to the hydrodynamic pressure force and the buoyant force. The transport equations of the turbulent kinetic energy and the specific turbulence dissipation rate specified in Mentor's SST model[10] are solved to estimate the eddy viscosity (ν_t). The flow variables are resolved by clustering the grids near the wall. Therefore, wall functions are not used.

For the spatial discretization of the complicated 3-D geometry, multiples of curvilinear, non-orthogonal, structured grids are overlapped, and weights are imposed for the overlapped cells. SUGGAR external library is active at every time step for cutting unnecessary volume grids and interpolating the boundaries of the trimmed volume grids. When the grid point is regarded as blanked due to the cutting process, the flow variables become zeroes inducing the sparse matrix during the algebraic formulation. When the grid becomes active again owing to grid transformation at the future time step, the variables are interpolated from the adjacent active grids and then iteratively solved together. On walls, weights are computed only once during the pre-process utilizing another external library USURP. The surface grids do not deform, and the wall overlaps remain the same throughout the simulation.

The free-surface is modelled with the single-phase level-set (Φ) method. For a stable computation, the equation is not solved in the region closer than $3\times 10^{-4}L$ from the wall, which is 0.81 mm in the current study. For the pressure velocity coupling, the projection method is used. The grids are closely divided into 0.11×10^6 grid points and are distributed to CPUs. The boundary data on each CPUs are interchanged using Message Processing Interface (MPI).

The components of the forces and moments considered are frictional, hydrodynamic, buoyant and gravitational forces, which are subscribed with the letter "F", "D", "B" and "G" next to the variables when reported. When the frictional, hydrodynamic, and buoyant forces are integrated at the wall, the grid surface is triangulated. The gravitational force is applied as a point value at the center of rotation.

Bi-conjugate gradients stabilized solver is used via PETSC for solving the formulated algebraic equation with the Block Jacobi pre-conditioner and the ILU local pre-conditioner.

The code algorithm is like the following: (1) each time step starts by moving the grids of ship and appendages with the increment of motions predicted from the previous time step, (2) SUGGAR performs a new interpolation, and the inner-loop recurs for 2-4 times, (3) inside the inner-loop, turbulence variables, level-set, velocities, and pressure are iteratively computed inside their own loops, (4) once the inner-loop ends, forces and moments are calculated based on the new flow field, and the corresponding motions are derived.

The whole simulations are performed in Gordon and Conrad NAVY-DSRC HPCs, and Neon HPC established from the University of Iowa.

3.2 *Grid*

Table 3 presents the summary of grid usage: for the fully assembled grid system utilized during self-propulsion and maneuvering simulations, total grid points consist of 1.02×10^8, 3.6×10^7 and 1.2×10^7 are used for the fine $(g1)$, medium $(g2)$, and coarse grid $(g3)$ which are distributed to 897 343 and 116 CPUs. Detailed information on each grid block is reported in Table 4.

Table 3 Total grid usage

Case	Total num. of grids (10^6) (Total num. of CPUs)		
	$g1$	$g2$	$g3$
POT	28 (250)	10 (96)	3.4 (28)
SP, TC	102 (897)	36 (343)	12 (116)

The grid generation is conducted manually by using Gridgen version 15. In the surface grid generation step, 2-D Cartesian grids are projected onto the three-dimensional database, and the internal grid points are aligned by solving the elliptic equation to maximize the orthogonality. When the database is wrapped with multiples of 2-D surface grids, the grids are allowed with overlap, and the overlap region shares at least three grid points with the adjacent surface grids. Volume grids are then genera- ted by marching the surface grids towards the outer flow region with an expansion rate of 1.12-1.15. The hyperbolic equation is solved during the extrusion to keep the high orthogonality. The overlap between volume grids should have at least three shared grid points as the surface grid.

Ten different blocks are overlapped for either side of the bare-hull, i.e., portside and starboard, and are mirror copied for the generation of the other side, as shown in Fig. 1. A large single grid covers from forward perpendicular to the near stern region of the bare-hull and the rest of concave or convex regions are overlapped with relatively small-sized grids. It is often regarded as conventional to avoid using several overlaps to minimize the interpolation between the volume grids. However, the extrusion process often requires random marching coefficients for solving the hyperbolic equations and consequently generates low-quality grids when a single grid embracing the arbitrary shape is used for the extrusion. The overall amount of interpolation has increased in the current study. However, the current approach aims to produce fewer skewed grids and streamlining the volume grid extrusion process. The target scaled wall distance (y^+) is less than two:

$$y^+ = \frac{\Delta s U^*}{\nu}, \quad C_F = \frac{0.026}{Re^{1/7}} \tag{2}$$

where Δs is the grid spacing normal from the wall, U^* is the frictional velocity scaled with respect to the wall shear stress $(=\sqrt{\tau_w/\rho}=\sqrt{C_F\rho U^2/2})$, Re is the Reynolds number based on the characteristic length and the inlet velocity (U).

The grid generation process for the rudder is more sophisticated than the process performed on the bare-hull due to the complicated shape of the rudder and the small gap existing between the rudder stock and the moving rudder. Applying multiple grids is unavoidable. Six and seven different blocks are used for either side of the rudder stock and the moving rudder, respectively, as shown in Fig. 2. For a practical simulation, the rudder gap is enlarged by a small distance to avoid excessive computational time during the interpolation process. The amount of deformation is considerably small, not to affect the flow physics near the rudder. More than six different 3-D Cartesian grids are added to complement voids or orphans appearing inside the rudder gap. Once the connectivity of the rudder grid is confirmed, cases in which the rudder angle deviates from zero are also tested to confirm their stable interpolation: the rudder angle is increased by two degrees up to maximum deflection, and every case is ensured with the absence of the voids or the orphans.

Propeller blades are composed of two different volume grids, as shown in Fig. 2, to refine the tip of the blade additionally. Only one volume grid is used for the propeller hub.

After generating each volume grid, refinement grids are located to increase the overall resolution of a specific region and isolate a specific grid assembly, e.g., propeller, rudder, and ship grid assemblies, as much as possible. The grid spacing of the refinement grid is usually more refined than the adjacent assembly. The refinement grid surrounds the parts having some margins to prevent the interpolation between the assembly and the grids located outside from the refinement grid. The propeller refinement

Table 4 Grid assembly composition ($g3$)

Name	Sub-part	i	j	k	ijk (10^6)	Num. of CPUs	Position[2]
BH	Wave-breaker	97	46	43	0.19	1	Sb, Pt
	Bow-Upper	36	49	58	0.1	1	Sb, Pt
	Bow-Lower	36	47	48	0.08	1	Sb, Pt
	Middle-body	126	47	105	0.62	5	Sb, Pt
	Stern-Upper	41	48	75	0.15	1	Sb, Pt
	Transom-wrap	17	49	75	0.06	1	Sb, Pt
	Transom-fill	26	49	26	0.03	1	Sb, Pt
	Stern-Lower	26	44	51	0.06	1	Sb, Pt
	P-root-wrap	34	40	61	0.08	1	Sb, Pt
	P-root-fill	16	33	26	0.01	1	Sb, Pt
RS	RS-Front	37	38	92	0.13	1	Sb, Pt
	RS-Upper	61	34	52	0.11	1	Sb, Pt
	RS-Mid	35	38	126	0.17	1	Sb, Pt
	RS-Mid-Comp	26	38	30	0.03	1	Sb, Pt
	RS-Lower	91	38	38	0.13	1	Sb, Pt
	RS-LowerU	41	26	35	0.04	1	Sb, Pt
MR	MR-Upper	81	41	46	0.15	1	Sb, Pt
	MR-UpperWrap	81	42	31	0.11	1	Sb, Pt
	MR-Lower	66	40	56	0.15	1	Sb, Pt
	MR-Back	47	43	28	0.06	1	Sb, Pt
	MR-Mid	36	37	39	0.05	1	Sb, Pt
	MR-MidU	66	30	36	0.07	1	Sb, Pt
	MR-MidL	81	27	36	0.08	1	Sb, Pt
PROP	Prop.-Hub	59	31	216	0.40	3	Center
	Prop.-Blade	81	33	60	0.16	1	Axisym.
	Prop.-BladeTip	50	33	65	0.11	1	Axisym.
REF	Ref.-POT[1]	100	100	100	1.00	9	Center
	Ref.-RS-1	71	29	29	0.06	1	Sb, Pt
	Ref.-RS-2	29	29	71	0.06	1	Sb, Pt
	Ref.-RS-3	35	29	29	0.03	1	Sb, Pt
	Ref-MR-1	42	57	57	0.14	1	Sb, Pt
	Ref.-MR-2	42	57	51	0.12	1	Sb, Pt
	Ref-MR-3	41	57	57	0.13	1	Sb, Pt
	Ref.-Prop	181	46	31	0.26	2	Center
	Ref.-Stern	128	72	126	1.16	10	Center
	Ref.-Ship	158	66	161	1.68	15	Center
BG	BG-POT[1]	97	84	84	0.68	6	Center
	BG-Calm	125	81	113	1.14	10	Center

Note: [1]Used for the propeller open-water simulation only, [2]Sb: Starboard, Pt: Port side, Axisym.: Axisymmetric.

grid covers the entire propeller assembly and rotates with the propeller ensuring consistent interpolation with the propeller. Similarly, the stern refinement grid covering three parts: propeller assembly, the rudder assembly, and the stern, enhances the overall resolution from the propeller inflow to the transom and the grid moves with the ship. The ship refinement grid covers the entire ship and has fine, vertically clustered resolution to capture the deformed free-surface close to the ship accurately and is connected to the background grid. The ship refinement grid does not move with the ship.

Initially, the fine grid is generated, and the distances of the internal points are coarsened with the ratio of $\sqrt{2}$ for all three curvilinear directions. The traces of the edges are retained during the coarsening stage. The coarse grid, which has gone through twice of the coarsening, is essentially the one-point skipped version of the fine grid, and the geometry is considered less deformed than the medium grid and has better grid quality. The capability of the coarse grid in resolving the flow physics is considered accurate. Some of the grid distances measured from the coarse grid are listed in the following statements: For the background grid, the equidistant grid is spaced vertically between $z = \pm 8.37 \times 10^{-3} L$ with the spacing value of $4.5 \times 10^{-4} L$. The covering range and the spacing are designed to include 20 grid points within the minimum and maximum range of the free-surface elevation distribution, shown from the previous KCS self-propulsion experiment or simulation, and marginal space is also considered to accommodate the appearance of unexpectedly high free-surface during the turning. The vertical distribu-

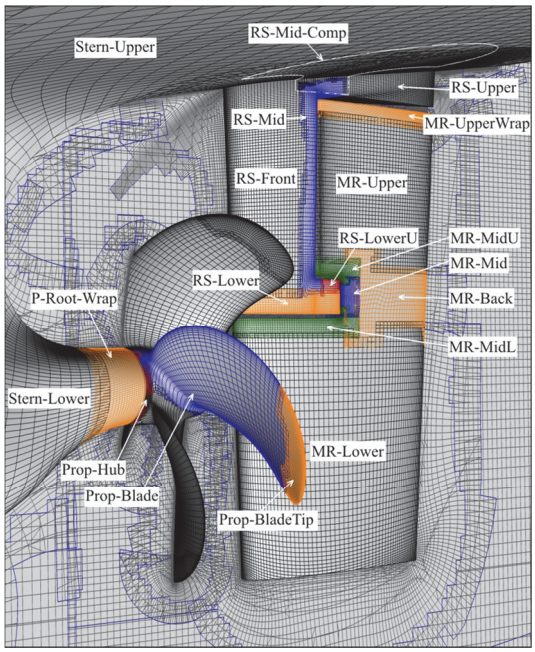

Fig. 2 (Color online) Grid composition of the propeller and rudder assemblies ($g3$, $y=0$ plane is shown)

tion of the ship refinement grid is designed to have 80% spacing than the background grid, and the distribution range is doubled since the grid is much nearer to the ship. The lateral spacing of the background grid is $0.02L$ for each direction, and the ship refinement grid has half of its spacing. The vertical spacing of the bare-hull is less than $1.85\times10^{-3}L$, which is 5 mm in model scale, and the uniform spacing is applied from the keel to deck height, not being clustered near the free-surface, to maintain a similar prediction accuracy even when the large roll appears. The longitudinal spacing of the bare-hull is $0.012L$ at maximum, and the maximum value appears at the midship.

3.3 *Computation domain and boundary conditions*

The computational domain is shown in Fig. 3. For the propeller open-water simulation, the distances from the propeller to the inlet, outlet, and sides are $5.0D_P$, $27.0D_P$ and $5.5D_P$. The entire domain is translated to deep water, not to experience the effect of free-surface. For the resistance, self-propulsion, and maneuvering simulations, the inlet, outlet, bottom, top and sides are away from the ship by $1.2L$, $2.0L$, $1.5L$, $0.5L$ and $1.5L$ all respectively, and the free-surface locates at $z=0$. Enlarging the domain size is tested during the resistance test, and the result showed negligible improvement.

Detailed information about the boundary conditions used in the current study are listed in Table 5. The reference hydrodynamic pressure is set to zero at both the inlet and the bottom. The curvatures of velocity components are set to zero at the outlet. A small amount of turbulent kinetic energy and turbulence dissipation rate are imposed at the inlet. On the wall, the velocities are the time derivative of the translational motions seen from the inertial frame, and the specific turbulence dissipation rate value is imposed as Mentor[10] proposed. The rests are all imposed with zero gradients (ZG).

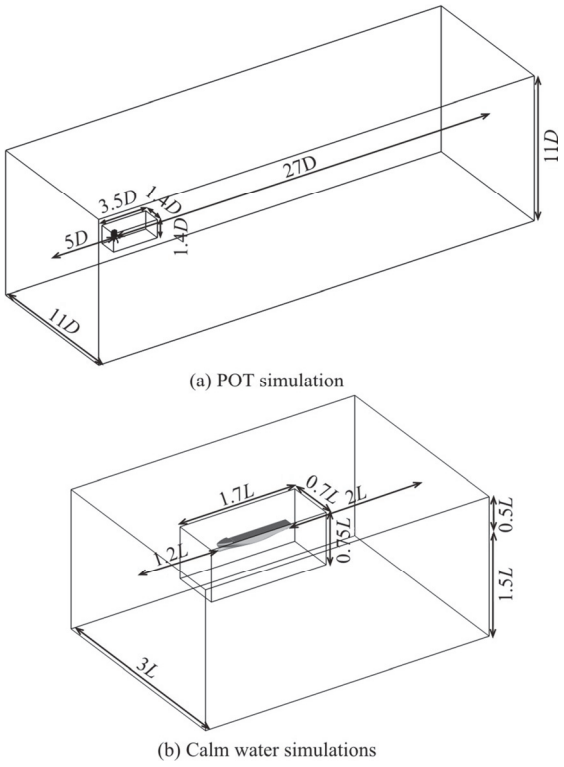

Fig. 3 Computational domains

Table 5 Boundary conditions

Boundary	u	v	w	p	k	ω	Φ
Wall	$\partial x/\partial t$	$\partial y/\partial t$	$\partial z/\partial t$	-	0	$60/(Re\beta_1 y^{+2})^*$	ZG
Inlet	U	0	0	0	10^{-7}	9	$-z$
Outlet	$\partial^2/\partial n^2=0$	$\partial^2/\partial n^2=0$	$\partial^2/\partial n^2=0$	ZG	ZG	ZG	ZG
Bottom	ZG	ZG	ZG	0	ZG	ZG	0
Top	ZG	ZG	ZG	ZG	ZG	ZG	ZG
Side	ZG	ZG	ZG	ZG	ZG	ZG	ZG

Note: * $\beta_1=0.075$.

3.4 *Discretization schemes*

The second-order central differencing scheme is used for the diffusion term of the momentum equations. For the convection term of the momentum equation, the fourth-order upwind scheme is used at the inner fluid region and is switched to the second-order upwind scheme at the boundaries. For the turbulent kinetic energy, specific turbulence dissipation rate, and the level-set function, the second-order upwind scheme is used for the convection term and is changed to the first order at the boundaries similar to the treatment imposed for velocities. All the temporal terms in momentum, turbulence, and level-set equations are discretized with the second-order implicit Euler backward scheme.

3.5 *Motion prediction*

Motions are explicitly predicted as a result of using very small time step. The motion prediction is performed only once when the new flow field is computed. Inside the inner loop of motion prediction, the 6DOF accelerations $(\boldsymbol{a} = \dot{u}, \dot{v}, \dot{w}, \dot{p}, \dot{q}, \dot{r})$ are calculated by consecutively solving the equation of motion formulated in the inertial frame:

$$m(\dot{u} - vr + wq) = X_{\mathrm{BH}} + X_{\mathrm{RS}} + X_{\mathrm{MR}} + X_{\mathrm{PROP}} \tag{3}$$

$$m(\dot{v} - wp + ur) = Y_{\mathrm{BH}} + Y_{\mathrm{RS}} + Y_{\mathrm{MR}} + Y_{\mathrm{PROP}} \tag{4}$$

$$m(\dot{w} - uq + vp) = Z_{\mathrm{BH}} + Z_{\mathrm{RS}} + Z_{\mathrm{MR}} + Z_{\mathrm{PROP}} \tag{5}$$

$$I_x\dot{p} + (I_z - I_y)qr = K_{\mathrm{BH}} + K_{\mathrm{RS}} + K_{\mathrm{MR}} + K_{\mathrm{PROP}} \tag{6}$$

$$I_y\dot{q} + (I_x - I_z)rp = M_{\mathrm{BH}} + M_{\mathrm{RS}} + M_{\mathrm{MR}} + M_{\mathrm{PROP}} \tag{7}$$

$$I_z\dot{r} + (I_y - I_x)pq = N_{\mathrm{BH}} + N_{\mathrm{RS}} + N_{\mathrm{MR}} + N_{\mathrm{PROP}} \tag{8}$$

The velocities $(\boldsymbol{v} = u, v, w, p, q, r)$ are obtained with the eight points averaged linear integration for which the increment is the average of accelerations obtained from the eight consecutive time steps:

$$\boldsymbol{v}_t = \boldsymbol{v}_{t-1} + \Delta t \frac{\sum_{N=0}^{7} \boldsymbol{a}_{t-N}}{8} \tag{9}$$

The velocities are then linearly integrated, similar to the acceleration for the derivation of the motions $(\boldsymbol{r} = x, y, z, \phi, \theta, \psi)$. The velocities from the four consecutive time steps are smoothed and used as the increment:

$$\boldsymbol{r}_t = \boldsymbol{r}_{t-1} + \Delta t \frac{7\boldsymbol{v}_t + 3\boldsymbol{v}_{t-1} + 3\boldsymbol{v}_{t-2} - \boldsymbol{v}_{t-3}}{12} \tag{10}$$

3.6 *Tolerance and others (for g3)*

Every flow variable iteratively converges inside its own non-linear iteration. The maximum number of iterations and the tolerances for the scaled velocities, pressure, turbulent kinetic energy, turbulence dissipation rate, level-set, and motions are 40, 150, 6, 50, 100 and 10^{-5}, 10^{-6}, N/A, N/A, 10^{-6}, 10^{-15}, respectively. The tolerance for the turbulent kinetic energy is not set for its fast convergence, while for the specific turbulence dissipation rate, setting the tolerance is trivial for its large residual value $(O(1))$. The residuals of velocities and pressure mostly reside at the $O(10^{-4})$ to $O(10^{-3})$ when the flow is stabilized after the initial conditions. The inner loop, looping each iteration of flow variables inside the time loop, is performed three times per time step. The time cost for SUGGAR, inner-loop and the motion prediction results in total 33 s to 38 s per time step, each spending about 2 s, 5 s to 8 s and 8 s. Relaxation factors for the momentum and pressure are set to 0.8 and 0.9.

3.7 *Controller*

The PID controller utilized for the prediction of the propeller rotational speed and rudder deflection angle are essentially having an identical form:

$$n(t) = K_{nP}e_n + K_{nI}\int_0^t e_n \mathrm{d}t + K_{nD}\frac{\partial e_n}{\partial t} \tag{11}$$

$$\delta(t) = K_{\delta P}e_\delta + K_{\delta I}\int_0^t e_\delta \mathrm{d}t + K_{\delta D}\frac{\partial e_\delta}{\partial t} \tag{12}$$

where $e_n = u - u_{\mathrm{target}}$, $e_\delta = \psi - \psi_{\mathrm{target}}$.

3.8 *Local coordinates*

The origin of the ship is at the center of rotation, which is set the same as the center of gravity in the current study. For the ship assembly, the longitudinal coordinate is positive from aft to forward, and the lateral coordinate is positive to the starboard. The vertical coordinate is positive downward. The local coordinate for the rudder is omnidirectional and is positive upward meaning the rudder angle and the angle of attack become positive when the trailing edge of the rudder locates at the starboard.

4. Results

4.1 *Propeller open-water simulation*

The predicted time series of the axial force and the axial torque, computed respect to the propeller axis, are scaled to thrust and torque coefficients:

$$K_T = \frac{T}{\rho n^2 D_P^4} \tag{13}$$

$$K_Q = \frac{Q}{\rho n^2 D_P^5} \tag{14}$$

The time series are averaged over enough time duration for the extraction of the mean values. Since the propeller is fully submerged and the motions are fixed, the buoyant force and the gravitational force are balanced remaining only frictional and hydrodynamic forces act on the propeller surface. The time series of the propeller open-water efficiency is calculated with the time series of thrust and torque coefficients:

$$\eta_0 = \frac{J}{2\pi}\frac{K_T}{K_Q} \tag{15}$$

The advance ratio is defined as follows:

$$J = \frac{U}{nD_P} \tag{16}$$

Table 6 provides validation results, and Fig. 4 displays the simulation and experiment values for comparison. The simulation is under-predicting all three variables, and the trend is identical for the grid triplet. The errors, defined from Formula (17), are small for the thrust coefficient by showing 1.7%, 1.0% and 0.99% on average for the fine, medium, and coarse grid. The errors for the torque coefficient are in the acceptable range. However, the values are mostly 2.2-3.4 times higher than those for the thrust coefficient by showing 4.2%, 3.4% and 2.2% error on average for the grid triplet, indicating that the lateral and vertical forces are predicted less accurate.

$$\text{Error}\,(\%) = \frac{\text{Exp.} - \text{CFD}}{\text{Exp.}} \times 100 \tag{17}$$

The error trend of both thrust and torque coefficient with respect to the advance ratio shows that the error deviations at the advance ratio of 0.4-0.8 are not significant at a higher advance ratio range, indicating the possibility of having a biased error.

The error trend with respect to the grid resolution reveals that the difference of the grid triplet solutions (ε_{21}, ε_{32}) for the thrust coefficient and the torque coefficient are both small by showing 0.9%-1.6% of fine grid solution values on average and are showing similar values. The trend supports the fact that the

Table 6 Validation of propeller performances (POT)

Var.	J	Exp.	CFD			U_1%$g1$	ε_{21}%$g1$	U_{32}%$g1$	Conv.	Error		
			$g1$	$g2$	$g3$					$g1$	$g2$	$g3$
K_T	0.10	0.458	0.457	0.448	0.437	0.10	–2.0	–2.3	MC	–0.3	1.4	2.90
	0.20	0.412	0.414	0.410	0.408	0.03	–0.9	–0.4	MD	–1.3	–0.4	–0.20
	0.40	0.316	0.313	0.310	0.312	0.03	–0.9	0.7	OD	–0.5	0.6	–0.10
	0.60	0.213	0.207	0.208	0.207	0.20	0.4	–0.3	OD	1.0	1.1	1.40
	0.70	0.158	0.154	0.155	0.155	0.40	0.6	0.1	MD	1.3	1.3	1.40
	0.75	0.130	0.127	0.128	0.128	0.80	0.9	0.4	MD	1.5	1.2	1.00
	0.80	0.102	0.099	0.100	0.101	0.70	1.4	0.7	MD	1.6	0.8	0.20
	0.90	0.044	0.041	0.044	0.045	2.30	5.5	2.2	MD	6.1	1.4	–0.80
	Ave.	-	-	-	-	**0.60**	**1.6**	**0.9**	**-**	**1.7**	**1.0**	**0.99**
$10K_Q$	0.10	0.698	0.688	0.679	0.674	0.10	–1.3	–0.7	MD	1.7	2.7	3.0
	0.20	0.641	0.623	0.622	0.626	0.03	–0.3	0.7	OC	2.3	2.6	1.7
	0.40	0.518	0.492	0.493	0.500	0.03	0.1	1.6	MC	4.1	4.1	2.7
	0.60	0.384	0.363	0.366	0.368	0.20	0.8	0.6	MD	4.2	3.9	3.4
	0.70	0.313	0.295	0.299	0.302	0.30	1.1	1.3	MC	4.4	3.8	2.7
	0.75	0.276	0.261	0.264	0.269	0.50	1.4	1.7	MC	4.5	3.5	2.1
	0.80	0.238	0.225	0.230	0.234	0.40	2.1	2.0	MD	4.7	3.0	1.3
	0.90	0.161	0.148	0.155	0.159	0.80	4.5	2.9	MD	7.3	3.6	0.9
	Ave.	-	-	-	-	**0.30**	**1.4**	**1.4**		**4.2**	**3.4**	**2.2**
η_0	0.10	0.104	0.106	0.105	0.103	0.01	–0.7	–1.6	MC	–2.0	–1.2	–0.1
	0.20	0.205	0.211	0.210	0.208	0.01	–0.6	–1.2	MC	–3.7	–3.0	–1.9
	0.40	0.388	0.405	0.401	0.398	0.01	–1.1	–0.8	MD	–4.8	–3.7	–2.8
	0.60	0.528	0.544	0.542	0.538	0.05	–0.4	–0.8	MC	–3.4	–2.9	–2.0
	0.70	0.564	0.580	0.577	0.570	0.10	–0.5	–1.2	MC	–3.2	–2.6	–1.4
	0.75	0.564	0.580	0.577	0.569	0.30	–0.6	–1.3	MC	–3.2	–2.4	–1.1
	0.80	0.545	0.561	0.557	0.551	0.30	–0.7	–1.2	MC	–3.3	–2.4	–1.2
	0.90	0.394	0.399	0.403	0.401	1.50	1.0	–0.6	OD	–2.0	–2.7	–2.1
	Ave.	-	-	-	-	**0.30**	**0.7**	**1.1**	**-**	**3.2**	**2.6**	**1.6**

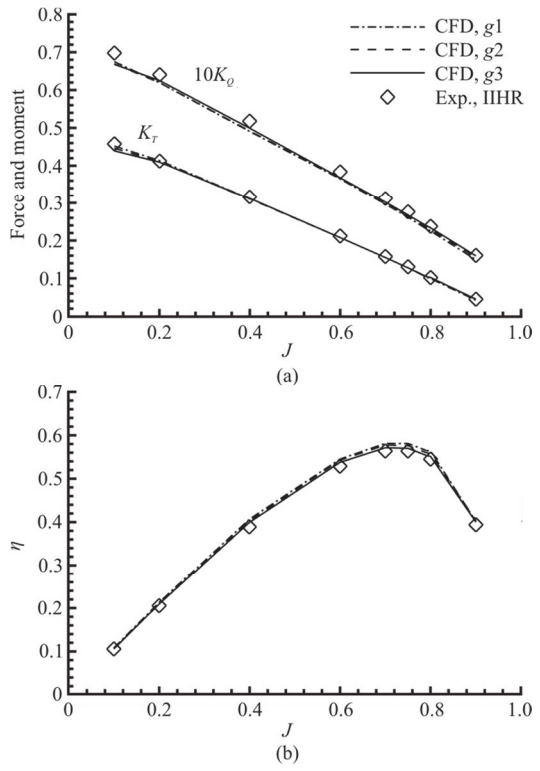

Fig. 4 Exp. and CFD propeller performances (POT)

torque coefficient is not sensitive to the grid resolution as much as the thrust.

The solution convergence is not smooth by showing only one and three monotonic convergence (MC) for the thrust coefficient and the torque coefficient. The small difference of the grid triplet solutions and the similar amount of iterative uncertainty (Formula (18)) are effective on the assessment of the grid convergence.

$$U_I = \frac{X_{\max} - X_{\min}}{2}, \quad X \text{ is any variable} \tag{18}$$

The propeller open-water efficiency errors are 3.2%, 2.6% and 1.6% for the fine, medium, and coarse grid, and the values are considered satisfactory. The errors are smaller than those from the torque coefficient since the torque coefficient is used as a denominator in Formula (15). The error trends with respect to the advance ratio and grid resolution are also similar to the ones shown from the thrust coefficient and torque coefficient. The solution convergence mostly showed monotonic convergence.

The predicted thrust coefficient and torque coefficients are fitted with the second-order polynomial:

$$K_T = t_2 J^2 + t_1 J + t_0 \tag{19}$$

$$K_Q = q_2 J^2 + q_1 J + q_0 \tag{20}$$

and coefficients are extracted for the use of thrust identification method in self-propulsion and maneuvering simulation sections. For $g3$, the coefficients are estimated as $t_2 = -0.11587$, $t_1 = -0.38774$, $t_0 = 0.4849$ and $q_2 = -0.01342$, $q_1 = -0.05084$, $q_0 = 0.0725$.

4.2 *Resistance simulation*

In the resistance simulation, the bare-hull is equipped with the rudder and towed in 2DOF. The axial and vertical components of the hydrodynamic, buoyant, and gravitational force predicted in the body-fixed frame are coordinate transformed to the inertial frame, and the resultant axial components in the inertial frame are summed up and scaled for the calculation of the residuary resistance coefficient:

$$C_R = \frac{X_D + X_B + X_G}{0.5\rho A_W U^2} \tag{21}$$

where A_W is the wetted area, ρ is the fluid density, and U is the inlet axial velocity. Friction force components are also moved to the inertial frame and scaled:

$$C_F = \frac{X_F}{0.5\rho A_W U^2} \tag{22}$$

The motion and residual force showed oscillations in the time series. Therefore, the mean values are obtained at the same last oscillations for the grid triplet. The frictional resistance for the experiment is calculated based on the 1957 ITTC frictional curve:

$$C_F = \frac{0.075}{(\lg Re - 2)^2} \tag{23}$$

Table 7 presents the validation result. The center of the rotation is submerged, and the bow is declined from the experiment, and the simulation predicts the same trend. The code over-predicts the sinkage, trim angle, frictional resistance and mostly under-predicts the residuary resistance and total resistance.

The errors for the sinkage are –6.6%, –5.5%, and –8.5% for the grid triplet, which are acceptable. The errors for the trim angle are relatively high, showing –39% on average. However, the prediction is still considered accurate enough since the magnitude of the trim angle is small by being less than 0.2°. The grid triplet is predicting the same trend with a small difference.

Table 7 Validation of motions and resistance components (resistance simulation)

Var.	Exp.	CFD			U_1%g1	ε_{21}%g1	U_{32}%g1	Conv.	Error		
		g1	g2	g3					g1	g2	g3
$100\sigma / L$	0.176	0.188	0.186	0.191	10.0	–1.1	2.7	OC	–6.6	–5.5	–8.5
τ	–0.122	–0.173	–0.166	–0.170	20.5	–4.1	2.3	OD	–41.5	–35.2	–39.2
$1000C_F$	–3.610	–3.682	–3.710	–3.652	0.3	0.8	–1.6	OC	–2.0	-2.8	–1.1
$1000C_R$	–1.054	–0.874	–0.996	–1.009	53.0	14.0	1.5	MD	17.1	5.5	4.2
$1000C_T$	–4.664	–4.556	–4.705	–4.661	10.3	3.3	–1.0	OD	2.3	–0.9	0.1
ω_D	-	0.613	0.617	0.621	-	0.7	0.7	MC	-	-	-

The maximum errors for the frictional resistance and the total resistance are –2.8% and 2.3% each, and the maximum differences of errors among grid triplet are 1.7% and 2.2%, which are considered small. The ability to resolve the velocity gradient near the wall is considered satisfactory for the current setup. The residuary resistance of the fine grid is predicted high compared to the rest of the grids. However, when the predicted residuary resistance is validated against to FORCE technology (FORCE) experiment value, which is –0.935, the error of the fine grid reduces to 6.5%. Accurate extraction of the mean value is affected by the large oscillations on time series. The domain size is enlarged, and the same simulation is performed. However, the domain size was not effective on the current result, which restates that the reflection was not prominent at the outlet. The duration of the current simulation is less than 10 s in real-time, and the damping is not used. As the simulation starts with the abrupt initial flow speed, the motion change is huge, and the solution seems to propagate during the integration of motion. Still, the simulations are considered practically good enough for the prediction of the mean total resistance.

The solution convergence path is often oscillatory, not monotonic. Although the solution differences are acceptable among grid triplets, the solution convergence is sensitively affected by the grid coarsening ratio and the overlap approach, which might have produced slightly different bare-hull geometry for the medium grid. Using a sufficient number of grids for the coarse grid also narrowed the solution difference between the coarse and medium grid.

A convergence of the propeller inflow is confirmed by performing the local flow study for the grid triplet. The velocity field is coordinate transformed from the inertial frame to the body-fixed frame. The vertical plane, whose longitudinal location is $0.975L$ from F.P., is extracted and shown in Fig. 5. The mean axial propeller inflow value, which is the average of the axial velocity at the propeller perimeter's inner side, is presented in Table 7. The thick boundary layer averaged inside the propeller perimeter presents about 62% of the ship speed. The convergence among the grid triplet is smooth, and the difference between the

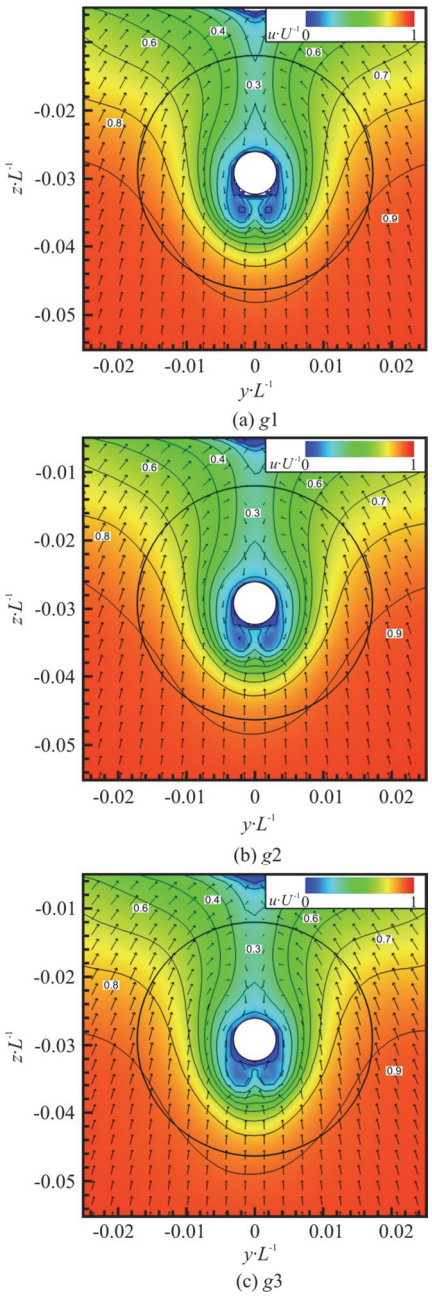

Fig. 5 (Color online) Propeller inflow (resistance simulation seen from the rear)

solutions from the fine grid and the coarse grid is about 1.3%, which indicates that the resolved boundary layer is satisfying for the coarse grid.

4.3 *Self-propulsion simulations*

For the validation of the self-propulsion simulation, the predicted time series of the heave, pitch, roll, propeller rotation speed, thrust coefficient, torque coefficient, advance speed and rudder angle are averaged during the quasi-steady-state for the extraction of the mean values. To get the time series of the torque coefficient, the cross product of the total force vector and the local displacement vector, which has its origin along the propeller axis, is performed on the propeller surface elements, and the axial component is summed and scaled. For the derivation of the self-propulsion factors, the thrust identification method is applied[1]. The approach assumes that the current thrust coefficient value is from the propeller open-water curve and derives the advance ratio and torque coefficient accordingly. The approach cannot assess the unsteady characteristics of the propeller performance caused by the non-uniform propeller inflow. However, the mean outcomes are considered accurate. The definitions of each self-propulsion factor with equations are described below. The open-water advance ratio (J_0) is the advance ratio at the uniform flow condition that produces the same amount of thrust coefficient predicted from the self-propulsion simulation:

$$K_T = t_2 J_0^{\,2} + t_1 J_0 + t_0 \tag{24}$$

Propeller open-water torque coefficient (K_{Q0}) is the corresponding torque coefficient at the same condition:

$$K_{Q0} = q_2 J_0^{\,2} + q_1 J_0 + q_0 \tag{25}$$

The propulsive efficiency (η) is the ratio between the power acting on the ship and the input propeller power. η can be divided into relative efficiency (η_R), propeller efficiency (η_P), and hull efficiency (η_H)

$$\eta = \frac{RU}{2\pi nQ} = \left(\frac{K_{Q0}}{K_Q}\right)\left(\frac{J_0}{2\pi}\frac{K_T}{K_{Q0}}\right)\left(\frac{1-t}{1-\omega_e}\right) = \eta_R \eta_P \eta_H \tag{26}$$

where the thrust deduction is the ratio of the mean resistance value (R) from the resistance simulation and the propeller thrust force (T) from the self-propulsion simulation $(1-t = R/T)$, and the effective wake fraction is the ratio of the open-water advance ratio and the advance ratio (J) from the self-propulsion simulation $(1-\omega_e = J_0/J)$.

The validation result for the motions, propeller rotational speed, thrust coefficient, torque coefficient, and the advance ratio is presented in Table 8. The validation result for the yaw angle is not shown since the course of the ship is straight and the value is very small. The experiment value for the heave is higher than the one from the resistance test, and the pitch angle is lower, and the simulation well predicts the trend. The predicted error for the motions is a little larger than the resistance simulation due to the complexity of the test condition, i.e., 6DOF instead of 2DOF and course keeping with the active rudder and active propeller.

Contrary to the resistance simulation, the code under-predicts the heave for the self-propulsion simulation. The error for the heave is 8.6%, 10%, and 5.0% for the grid triplet. The solution difference among the grid triplet is considered small. The roll angle is over-predicted and shows a negative sign, which means the ship leans to the portside, the same as the experiment. The errors for pitch angle and roll angle are high due to the small order of the values, and the grid triplet predicts similar values. The neutral rudder angle is predicted as a positive value, meaning the trailing edge of the rudder is located to the star-

Table 8 Validation of motions and propeller performances (SP test, steady-state)

Var.	Exp.	CFD			ε_{21}%g1	ε_{32}%g1	Conv.	Error		
		g1	g2	g3				g1	g2	g3
$100z/L$	0.220	0.201	0.198	0.209	–1.5	5.6	OC	8.6	10.0	5.0
θ	–0.090	–0.144	–0.141	–0.158	–2.1	12.1	OC	–60.8	–57.4	–76.4
ϕ	–0.120	–0.470	–0.590	–0.600	25.5	1.7	MD	–276.6	–372.7	–380.7
δ_N	0.750	0.630	0.750	1.520	19.0	102.7	MC	16.0	0.00	–102.7
n'	37.720	36.46	36.760	36.480	0.8	-0.8	OD	3.3	2.5	3.3
K_T	0.245	0.256	0.257	0.256	0.4	-0.4	OC	–4.5	–4.9	–4.5
$10K_Q$	0.397	-	0.438	0.428	-	-2.3	-	-	–10.3	–7.8
J	0.770	0.799	0.790	0.797	–1.1	0.9	OD	–3.8	–2.6	–3.5
Ave.	-	-	-	-	-	-	-	-	5.1	4.8

board as same as the experiment. The grid triplet solutions for the neutral rudder angle show larger deviations between the grids than the results shown from ship motions, i.e. the heave, pitch angle, and roll angle, which are calculated at a much larger scale. The convergence path is oscillatory convergence for the heave and pitch angle, similar to the resistance test result, while the roll angle and the neutral rudder angle show monotonic divergence and monotonic convergence. The effect of grid coarsening seems to be less for the roll angles than the heave and pitch angle.

The thrust coefficient from the experiment is much larger than the propeller open-water value at the measured advance ratio 0.77 due to the thick boundary layer appears at the propeller inflow and the predicted thrust coefficient is following the trend. The error for the thrust coefficient is larger compared to the propeller open-water simulation by being –4.5%, –4.9% and –4.5% for the grid triplet. The predicted propeller rotational speed is showing 3.3%, 2.5% and 3.3% error for the grid triplet, and the solutions are close to each other. The main difference between the propeller open-water simulation and the self-propulsion simulation is the existence of the bare-hull and the rudder. Therefore, the factors that affect the thrust coefficient during the self-propulsion simulation are: (1) the accuracy of the resolved ship boundary layer, which becomes the propeller inflow, (2) the accuracy of the resolved flow field where the interaction between the propeller and the rudder acts, (3) the accuracy of the controller, (4) the ship motions. The convergence with respect to grid resolution is confirmed for the factor 1 during the resistance simulation part. However, the validation against the experiment result is missing. Therefore, the local flow validation seems required to confirm the difference of the propeller inflow between the experiment and the simulation during the resistance test stage. The small error shown for the frictional force during the resistance simulation stage can partially support the validity of the resolved ship boundary layers near the wall. However, the accuracy of the boundary layer away from the wall is not guaranteed, which might appear as the penalty of using URANS. The impact of the factor 2 on the thrust coefficient is considered less dominant than the factor 1. However, the amount of effect is unknown, and the experiment data for the validation of factor 2 is not easy to achieve due to the complex geometry. The under-prediction of the propeller rotation speed results from over-predicting the thrust coefficient, which dominantly affects the advance speed, since the two variables are correlated under the constraint of the controller and the relationship, shown in Formulas (11), (16), and (19). Therefore, the assessment on the factor 3 is also required. The ship motions can affect the propeller inflow, and thereby, affect the thrust coefficient. The amount of effect due to factor 4 is not estimated. However, the amount is expected to be insignificant due to the small motion values.

The torque coefficients are over-estimated the same as the thrust coefficient. The errors for the torque coefficient are −10.3% and −7.8% for the medium and the coarse grid, which are almost doubled from the errors of the thrust coefficient similar to the propeller open-water simulation validation result. The post-processing of the torque coefficient for the fine grid is refrained due to the memory issue inside the post-processing code. However, the values are expected to be similar to the medium, and the coarse grid results since both the propeller rotational speed and the thrust coefficients are predicted very similarly. The convergence paths are oscillatory, similar to the resistance simulation, and only the thrust coefficient shows convergence.

A validation study on the self-propulsion factors, shown in Table 9, is performed with the results of the coarse grid. The open-water advance ratio shows a 5.2% error due to the error of the thrust coefficient shown from the self-propulsion simulation. The open-water advance ratio error contributes to an 8.3% error for the effective wake fraction. While the error for the thrust deduction is small, the error for the hull efficiency is large by showing −12.2%, which is significantly affected by the error of the effective wake fraction. The relative rotating efficiency is found to have a 6.3% error. The propeller efficiency and the propulsive efficiency are well predicted by showing 2.2% and –2.8% errors. The propeller efficiency is off from the optimal design value due to the thick ship boundary layer at the propeller inflow. The propulsive efficiency is estimated as 64%-66%. The general prediction accuracy for the self-propulsion factor is considered satisfactory considering the moderate averaged error, which is 5.6%.

A study for the local force and moment is performed to describe the force equilibrium within the body-fixed frame and confirm the neutral rudder angle effect, which is the main factor for the course-keeping. The method of the local force and moment study approach gives the identifiable number at the surface area of each assembly and integrates the forces separately. The moments are calculated based on the forces and the distances between the center of rotation of the ship and the centroids of each element composing the surface area. The result is shown in Table 10. The scaling factors for the forces are the same as Formulas (21) and (22). For the moments, the value is additionally scaled with the length of the ship. For the active moving rudder condition, the total forces and the total moments are showing negligible

Table 9 Validation of SP factors (SP test, steady-state, $g3$)

Var.	Exp.	CFD	Error
J_0	0.540	0.512	5.2
$1-\omega_e$	0.701	0.643	8.3
$1-t$	0.854	0.875	–2.5
η_R	1.072	1.004	6.3
η_P	0.495	0.484	2.2
η_H	1.218	1.367	–12.2
$\eta\,\eta$	0.646	0.664	–2.8
Ave.	-	-	5.6

Table 10 Balances of local forces and moments (SP simulation, steady-state, $g3$)

Case	Var.	BH*	RS	MR	PROP	TOT
SP (Active MR)	$1000X^*$	–5.008	–0.127	–0.163	5.325	0.028
	$1000Y^*$	–0.044	0.437	–0.281	–0.120	–0.007
	$1000Z^*$	–1.294	–0.155	–0.391	–0.361	–2.200
	$1000K^*$	0.027	–0.014	0.015	–0.026	0.002
	$1000M^*$	0.191	–0.079	–0.198	0.063	–0.023
	$1000N^*$	0.024	–0.209	0.135	0.051	0.001
SP ($\delta = 0$)	$1000X^*$	–4.994	–0.133	–0.155	5.311	0.028
	$1000Y^*$	–0.067	0.496	–0.027	–0.116	0.285
	$1000N^*$	0.028	–0.237	0.013	0.050	–0.147

Note: *The total gravitational force is assigned at BH.

amounts since the ship is in steady-state condition and not accelerated (the sum of the right-hand side of Formulas (3)-(8) become close to zero). However, the forces or moments exerted on each assembly are balancing with other assemblies. The surge force balance is clear. The bare-hull, rudder stock, and the moving rudder experience the resistance, and the propeller exerts the thrust force balancing the resistances. For the lateral force balance, the bare-hull, propeller, and moving rudder exert negative side force. Only the rudder stock cancels all the other forces by exerting a positive lateral force that is passively induced from the asymmetric propeller wake. For vertical force balance, all assemblies are producing the force downwards. However, the amount is negligibly small compared to the mass of the ship or the buoyant force whose orders are at around seven times $O(10^2)$. Therefore, the values are not valuable nor accurate. The roll moment produced from the bare-hull is not negligible and has the same amount as the value produced from the propeller. The roll moments of the rudder stock and the moving rudder are canceling out each other. The pitch moment produced by the propeller is positive, which may have induced a lower pitch angle for the self-propulsion test compared to the resistance test. The vertical force of the propeller is found to be negative, which induces the bow down. However, the axial force seems dominant when determining the positive pitch moment for the propeller. Having different shapes for the aft and forward have induced a positive pitch moment for the bare-hull. The rudder stock and the moving rudder induce a negative pitch moment, canceling the positive pitch moment induced from both the bare-hull and the propeller. The yaw moment induced from the lateral force of the rudder stock is canceled from the positive yaw moment exerted from the bare-hull, moving rudder, and the propeller, and the contribution of the moving rudder is the largest. The local force and moment balance at the steady-state cannot track the contribution of each assembly until the ship results in the final posture. If the local force and moment are recorded transitionally, the contribution of each assembly is expected to show up.

The same simulation is performed with the fixed zero rudder angle condition, and the local force and moment of the moving rudder are compared with the active moving rudder condition. The resistances that the rudder stock and moving rudder get change slightly. However, the overall surge force balance is not significantly changed. The lateral force and the yaw moment show distinct differences compared to the active moving rudder condition. The total lateral force becomes not negligible since the moving rudder does not exert enough force compared to the active moving rudder condition. Meanwhile, the lateral forces from the bare-hull and the propeller do not change significantly, which may infer that the newly

determined motions are not significantly changed from the previous condition. The yaw moment balance shows the same trend as the lateral force. The total yaw moment has a large negative value induced by the positive lateral force from the rudder stock. The moving rudder does not exert enough yaw moment necessary for the course keeping.

Perturbed pressure distribution on the rudder surface is displayed in Fig. 6 to confirm the difference of the lateral force on the moving rudder between the two conditions. For calculating the perturbed pressure distribution, the mean pressure distribution obtained from the active moving rudder condition is subtracted by the mean pressure distribution from the fixed zero rudder angle condition. The mean pressure on the portside of the rudder is higher than the mean pressure from the starboard and the distinct difference is prominent on the leading edge of the moving rudder than the rudder stock.

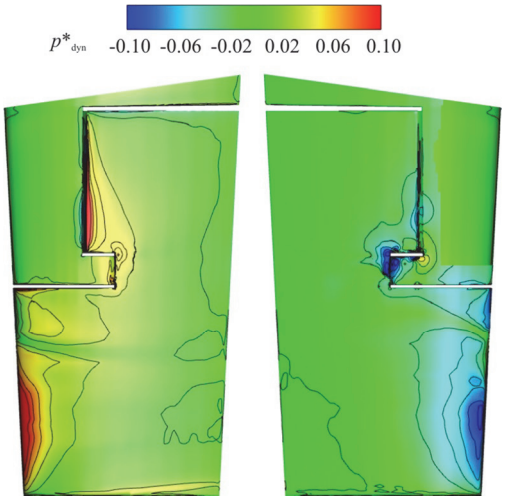

Fig. 6 (Color online) Perturbed mean dynamic pressure distribution on the rudder (Active RM result is subtracted by the $\delta = 0$ result)

A local flow study is performed to estimate the angle of attack on the leading edge of the rudder stock and the moving rudder. The velocity field is coordinate transformed to the body-fixed frame and averaged over enough duration during the steady-state. Also, the relative speed between the inertial frame and the body-fixed frame, which is mostly the advance speed for the current case, is added to evaluate the variables at the towing condition. The angle of attack is obtained by searching the stagnation point on the lateral planes extracted at different vertical locations, as shown in Fig. 7. The angle of attack distribution is shown in Fig. 8. In Fig. 8, the origin of the plot is set to the vertical location of the propeller axis for easy access, and the vertical distances between the ticks are one-fourth of the propeller diameter. Therefore, the positive vertical location data is the angle of attack calculated for the moving rudder and vice versa. For the fixed zero rudder angle condition, the angle of attack on the rudder stock is larger than 2.7°. The moving rudder gets a −1.5° angle of attack whose magnitude is the same amount as the predicted neutral rudder angle. As the moving rudder becomes active and deflects to the neutral rudder angle, a slight change of angle of attack is shown at the rudder stock. The angle of attack on the moving rudder increases closely to zero, exerting the lateral force by being favorable to the propeller wake shown in Fig. 9(b).

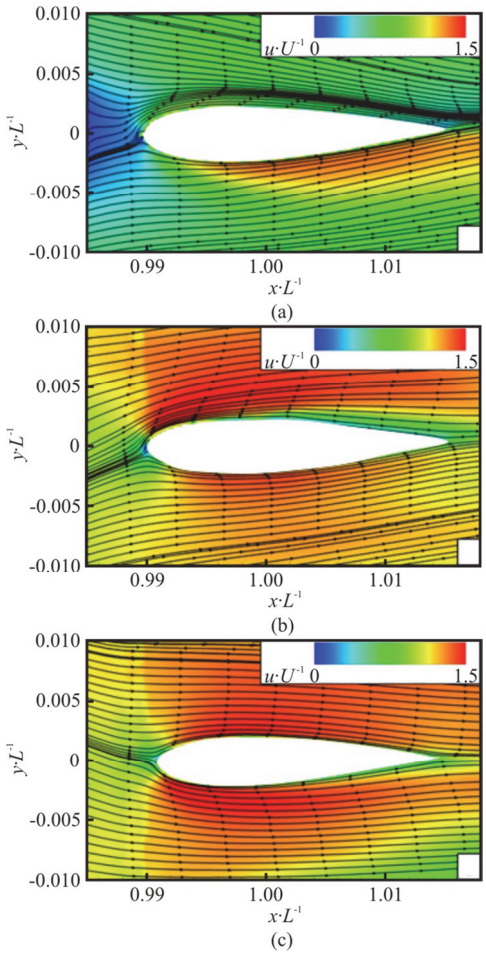

Fig. 7 (Color online) Mean local flow around the rudder at different vertical locations (SP simulation, steady-state, Active RM, $g3$)

Figure 9(b) is the vertical plane extracted at the longitudinal location of the propeller wake, which is $0.988L$ from the F.P. The characteristics of the mean propeller wake within the propeller perimeter could be found as two things: (1) stronger axial velocity on the starboard side, (2) the vortex pattern (shown as vectors), which is composed with the lateral velocity and the vertical velocity, rotating in clockwise as same as the direction of the propeller rotation and has larger

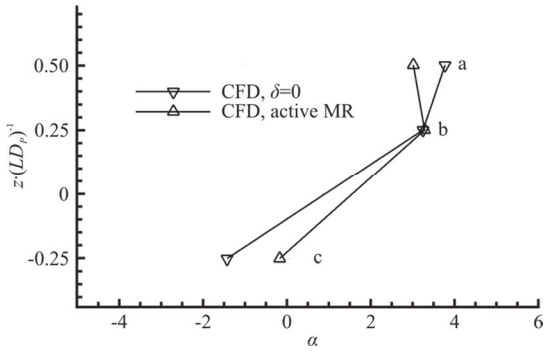

Fig. 8 Angle of attack distributions on the leading edge of rudder (SP simulations, steady-state, $g3$)

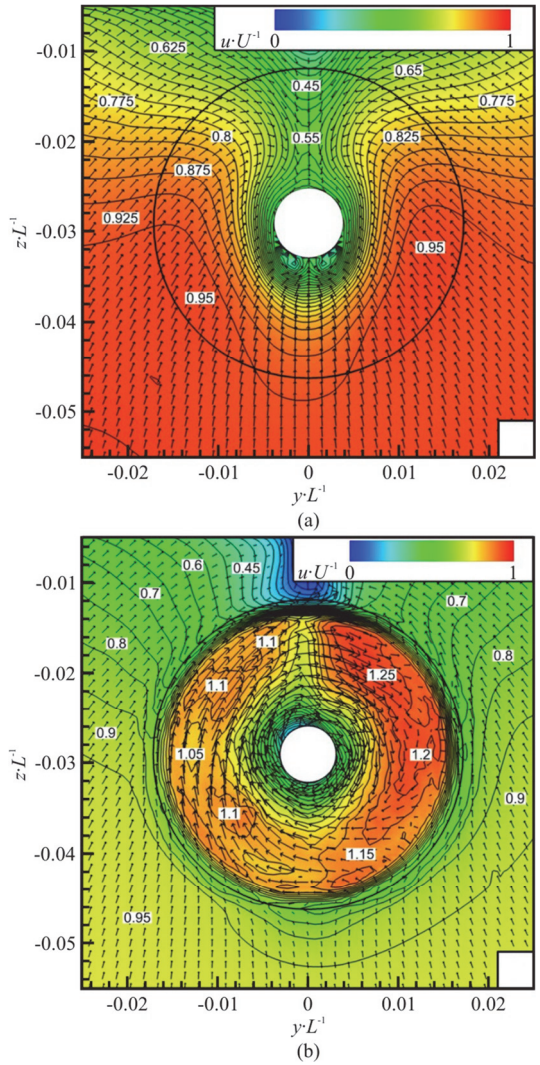

Fig. 9 (Color online) (a) Mean propeller inflow and (b) propeller wake (seen from the rear, SP simulation, steady-state, $g3$)

magnitude at the portside and the upper side. The dominant factor for inducing the angle of attack on the rudder stock and the moving rudder seems to be the vortex than the imbalance of the axial force, although the angle of attack is determined in the 3-D flow field since the signs and magnitudes of the obtained angle of attack can be explained with the direction and magnitude of the vortex: (a) the vortex at the upper region, where the lateral velocity is strong and positive, induces a large and positive angle of attack on rudder stock, (b) the vortex at the bottom region has a weaker and negative lateral velocity which induces small and negative angle of attack for the moving rudder during the fixed zero rudder angle condition.

For the investigation of the propeller wake, the correlation between the propeller wake and the time series of the forces of a single blade, shown in Fig. 10, is studied. In Fig. 10, the time series are matched with the location of the blade. The stronger axial velocity distribution on the starboard side of the propeller wake can be explained when referring to the thrust exerted from the blade: the thrust from a blade, which is considered to be a dominant factor for inducing the axial velocity, is higher during the starboard sweep (a-b-c) compared to the portside sweep (c-d-a′), on average. To explain the trend of the vortex, the time series of the lateral force and the vertical force is examined: (1) the lateral force and vertical forces are off-phase by 90°, (2) the lateral force is the maximum at the blade position (a) and (c), (3) the vertical force is the maximum at the blade position (b) and (d). The directions of the lateral and vertical force shown from the time series match with the direction of the vortex and confirm the acceleration of the flow towards propeller rotational direction in every azimuth angle, however, the acceleration occurs to the flow very near to the propeller and the flow seem to experience the additional effect from the adjacent vortex shown in Fig. 9(a), which cancels out the vortex at the starboard side and accelerates at the portside, consequently generating the flow field with weaker lateral velocity for the moving rudder than the rudder stock.

A correlation between the time series of the thrust and the propeller inflow distribution, shown in Fig. 9(a), is found to explain the thrust oscillation of a single blade. The longitudinal location of the propeller inflow plane is the same as the one from the resistance simulation, which is Fig. 5. The original hydrodynamic thrust force is decomposed with discrete Fourier transform (DFT) and the time series which are reconstructed with the major harmonics are also shown in Fig. 10. The characteristics of the mean propeller inflow distribution inside the propeller perimeter are: (1) the intensified and symmetric (to $y=0$ plane) axial velocity distribution, (2) the symmetric vortex (shown as vectors) favorable to the

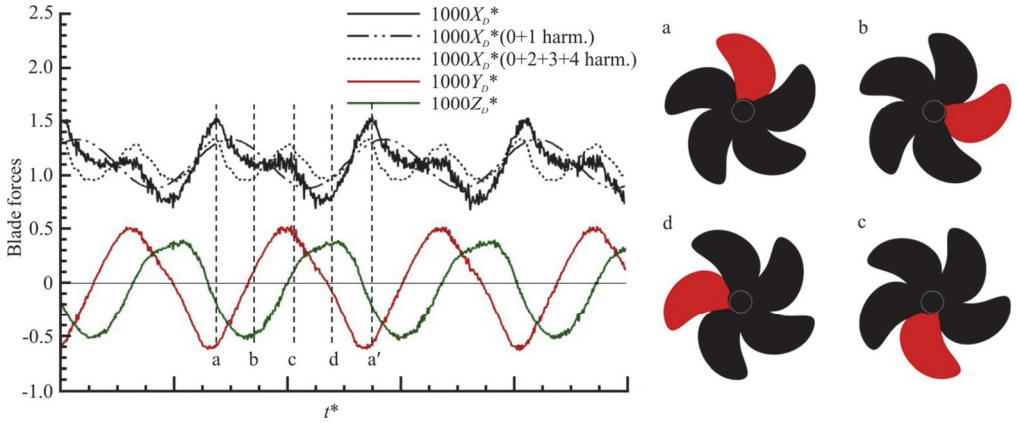

Fig. 10 (Color online) Time series of hydrodynamic forces of a blade and blade location (seen from the rear, SP simulation, steady-state, $g3$)

direction of propeller rotation in portside and unfavorable in starboard. The intensification of the axial velocity distribution compared to the resistance simulation is due to the propeller suction effect: the ω_D value is found as 0.785, which is $16\%U$ larger than the resistance simulation, and the symmetric vortex is due to the ship boundary layer converging along with the shape of the stern. The distribution of the axial velocity inside the propeller perimeter provides different advance ratio conditions for a blade during its rotation, and the corresponding harmonic frequency is expected to be near the double of the propeller rotation frequency since it is symmetric. As shown from the time series and the DFT result, shown in Fig. 11, the harmonic amplitudes of the thrust time series are dominant up to second harmonics, and the ratio of the second harmonic amplitude to the original oscillation amplitude (average of min and max from the original time series) is about 48%. A factor that induces harmonic amplitude at the rate of the propeller rotation frequency is more likely the vortex at the propeller inflow, whose directions are all different with the increase of the azimuthal angle. The first harmonic amplitude is 64% of the original oscillation amplitude, which is larger than the second harmonic amplitude by 16%. Meanwhile, the lateral force and the vertical force seems dominantly affected by the vortex since only the first harmonic is found dominant from their time series.

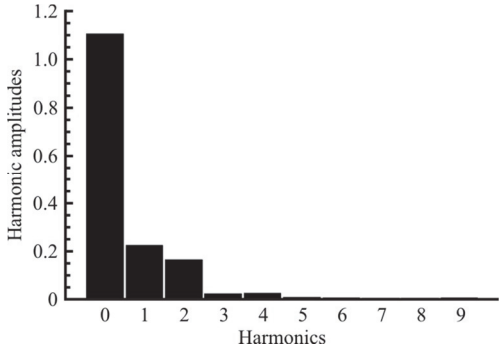

Fig. 11 Harmonic amplitudes of the hydrodynamic axial force of a blade (SP simulation, steady-state, $g3$)

4.4 *Turning circle simulations*

A similar process has been done for the +35 and -35 rudder deflected (starboard side TC (TC+35) and portside TC (TC-35)) steady-state turning simulations. The validation variables include the IMO criteria extracted from the trajectory and the motions and propeller performances averaged during the steady-state turning. Trajectories and time series are shown in Figs. 12 and 13, and the validation result is shown in Table 11. Since the medium grid predicts a very close result to the coarse grid, only the result predicted by the coarse grid undergoes the validation study. The difference of variables between the portside and the starboard turning is also estimated and assessed.

The overall errors for the IMO criteria: advance (Ad), transfer (Tr), tactical diameter (TD), and accumulated time when the ship arrives at each state $(t^*_{Ad} = t^*_{Tr}, t^*_{TD})$, are in the acceptable range by showing 8.8%, 2.9% of average errors for the portside and starboard turning. The variables for the portside turning are over-predicted, while the variables for the starboard turning are mostly under-predicted with small errors. Also, the difference of the IMO criteria between the portside and the starboard is much more significant than the experiment by showing a 10.2% difference on average compared to the 2% difference obtained from the simulation.

The overall prediction accuracy for the motions is in an acceptable range considering the complexity of the test condition. The averaged errors for the motions are 29.6% and 16.3% for the portside and

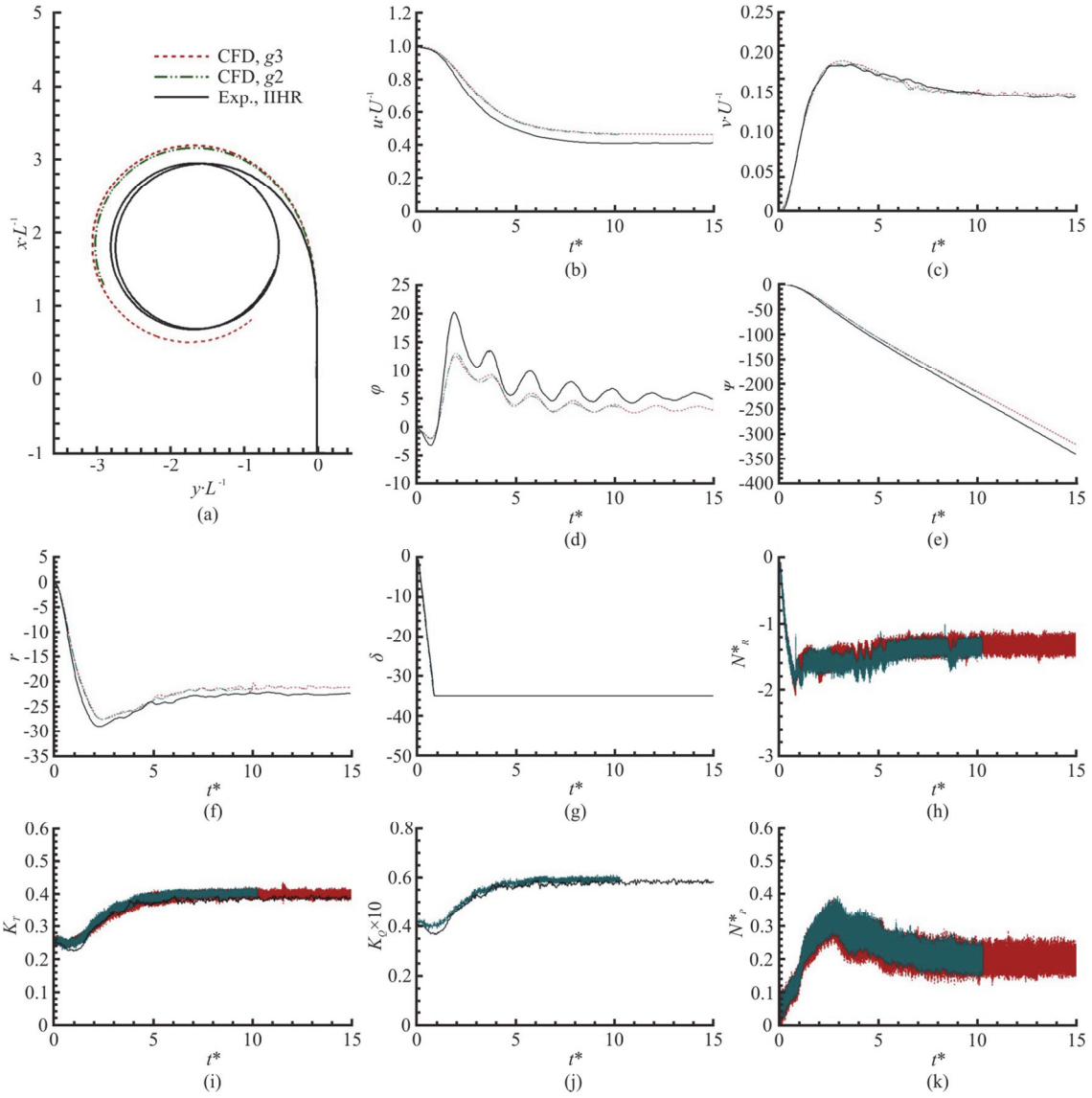

Fig. 12 (Color online) Trajectory and time series of Exp and CFD (TC-35)

starboard turning. The following descriptions give more information about each error compared to the error shown from the self-propulsion simulation. The heave is under-predicted as same as the self-propulsion and shows 66.7% and 50% errors for the portside and starboard turning, which are five to six times larger than the error shown during the self-propulsion simulation although the magnitude of the heave has increased. The heave from the experiment indicates more submersion compared to the self-propulsion. Contrarily, the simulation is predicting the leaped heave. The roll angle, which is over-predicted during the self-propulsion simulation, is now under-predicted and shows 40.2% and 19.1% errors for the portside and starboard turning. The errors for the roll angle are decreased compared to the self-propulsion due to the dramatic increase of the magnitude of the roll angle. The pitch angle shows a similar trend to the roll angle. The pitch angle is over-predicted during the self-propulsion, the same as the roll angle. The portside turning shows under-prediction, and the starboard turning shows almost similar value to the experiment. The error for the pitch angle is 51.8% for the portside turning, which is similar to the self-propulsion, and axial velocity, the drift angle is under-predicted for both turnings with 9.8% and 6.3% errors, and the difference between the two turnings are –5.9% which less than the experiment value of –9.7%. The yaw rate is under-predicted with 20.5% and 15.4% errors for the two turnings and simulation shows less difference between the two turnings than the experiment.9.5% for the starboard turning. The magnitude of the pitch angle from the experiment is almost tripled for the

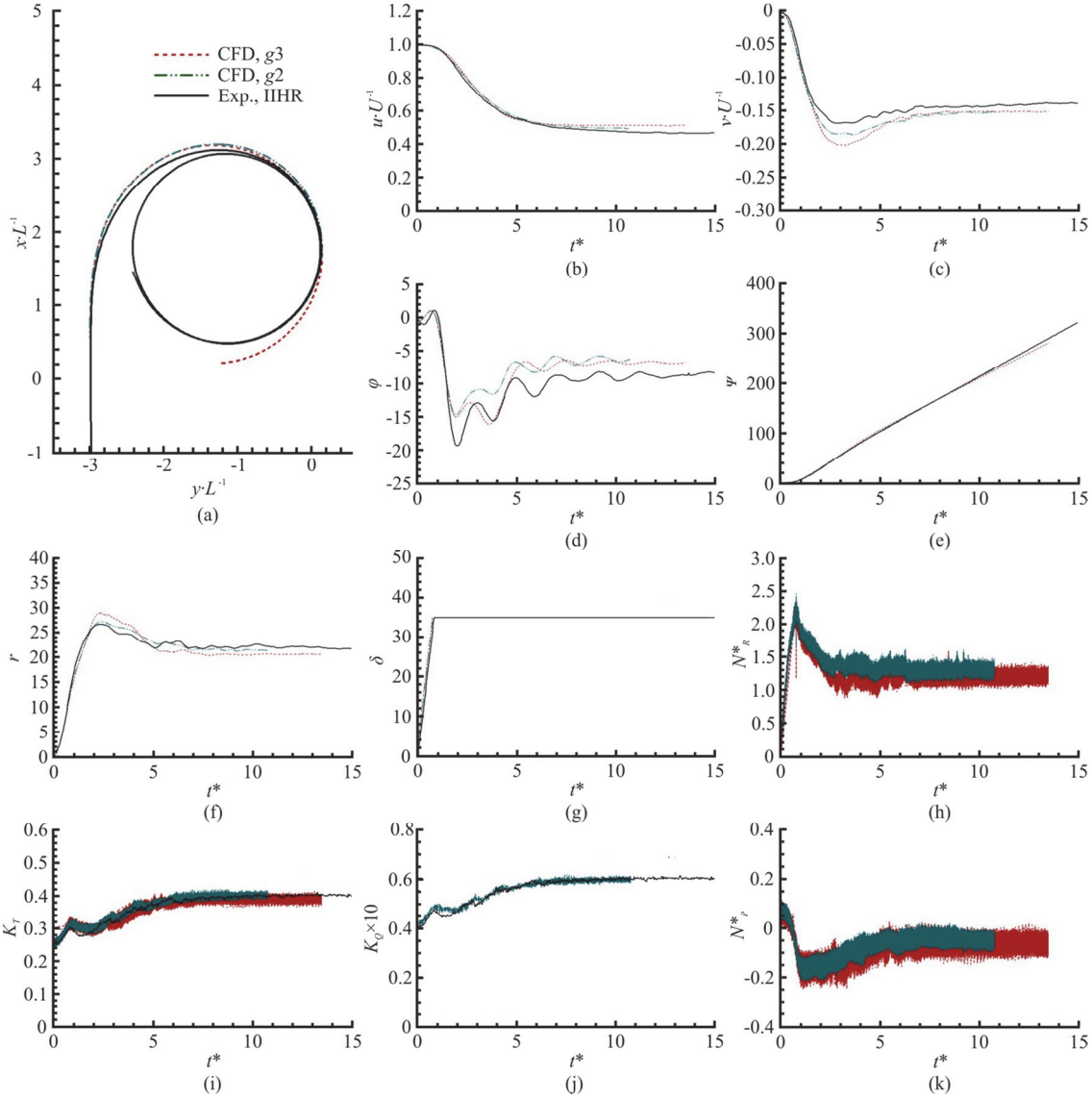

Fig. 13 (Color online) Trajectory and time series of Exp and CFD (TC+35)

portside turning compared to the self-propulsion, while the pitch angle from the simulation shows a very similar value. The magnitude of the pitch angle is a little increased for the experiment during the starboard turning, and the simulation shows a decrease with little amount. The difference between the two turnings is larger for the heave, and the pitch angle for the experiment and the simulation shows a larger difference for the roll angle. As the ship becomes to be in a state of a circular motion, four validation variables are additionally involved: axial velocity, lateral velocity, drift angle and yaw rate. The amount of axial velocity during the turning decreases drastically from the axial velocity shown from self-propulsion. It becomes 41%-47% of the self-propulsion value during the experiment and 46%-51% during the simulation. The simulation over-predicts the axial velocity for both portside and starboard turning by showing −9.7% and −12.6% errors, while the trend and the value difference between the two turnings are similar by being −11.8% difference for the experiment and −9.2% for the simulation. The lateral velocity increases to 13.9%-14.5% of the self-propulsion speed for the experiment, and the simulation predicts 14.7%-15.1%. The simulation over-predicts the lateral velocity with a −8.6% error for the portside turning and predicts a similar value for the starboard turning by showing a −1.4% error. The difference between the portside and the starboard turning for the lateral velocity is 4.2% for the experiment and −2.7% for the simulation, which is the opposite trend. Overall, the axial and lateral velocities are over-predicted, which means the speed loss is less than the experiment. Due to the over-prediction of the

Table 11 Validation and the difference between the turnings (TC±35 tests, steady-state, $g3$ for CFD)

Var.	Exp.			CFD			Error	
	TC-35	TC+35	Diff. %mean	TC-35	TC+35	Diff. %mean	TC-35	TC+35
Ad/L	2.870	3.060	6.4	3.120	3.1100	–0.3	–8.7	–1.6
Tr/L	–1.130	1.340	17.0	–1.260	1.2200	–3.2	–11.5	9.0
TD/L	–2.690	3.080	13.5	–3.000	3.0800	2.6	–11.5	0.0
t^*_{Ad}	4.090	4.390	7.1	4.340	4.2500	–2.1	–6.1	3.2
t^*_{TD}	7.880	8.440	6.9	8.350	8.4800	1.5	–6.0	–0.5
Ave.	-	-	10.2	-	-	2.0	8.8	2.9
$100z/L$	0.390	0.300	–26.1	0.130	0.1500	14.3	66.7	50.0
ϕ	5.270	–8.480	46.7	3.150	–6.8600	74.1	40.2	19.1
θ	0.309	0.126	–84.1	0.149	0.1380	–7.7	51.8	–9.5
u/U	0.465	0.413	–11.8	0.510	0.4650	–9.2	–9.7	–12.6
v/U	–0.139	0.145	4.2	–0.151	0.1470	–2.7	–8.6	–1.4
β	–19.400	17.600	–9.7	–17.500	16.5000	–5.9	9.8	6.3
r'	–0.876	0.794	–9.8	–0.696	0.6720	–3.5	20.5	15.4
Ave.	-	-	27.5	-	-	16.8	29.6	16.3
K_T	0.385	0.399	3.6	0.399	0.3820	–4.4	–3.6	4.3
$10K_Q$	0.579	0.600	3.6	0.582	0.5880	1.0	–0.5	2.0
J	0.320	0.348	8.4	0.37	0.4060	9.3	–15.6	–16.7
n'	38.00	38.00	-	36.48	36.4800	-	4.0	4.0
Ave.	-	-	5.2	-	-	4.9	5.9	6.7
J_0	0.258	0.229	–11.9	0.209	0.2470	16.7	19.0	–7.9
$1-\omega_e$	0.696	0.685	–1.6	0.494	0.6360	25.2	29.0	7.1
η_R	1.050	1.040	–1.0	1.0536	1.0054	–4.7	–0.3	3.3
η_P	0.261	0.233	–11.3	0.216	0.2540	16.2	17.2	–9.0
Ave.	-	-	6.4	-	-	15.7	16.4	6.8

axial velocity, the drift angle is under-predicted for both turnings with 9.8% and 6.3% errors, and the difference between the two turnings are –5.9% which less than the experiment value of –9.7%. The yaw rate is under-predicted with 20.5% and 15.4% errors for the two turnings and simulation shows less difference between the two turnings than the experiment.

Due to the speed loss during the turning, the mean propeller inflow distribution, shown in Fig. 17, has much less mean axial velocity compared to the self-propulsion. Therefore, the propeller operating condition at the very low advance ratio: the thrust and torque coefficient increase significantly, and the propeller efficiency drops. The increase of the thrust coefficient from the self-propulsion is 57%, 63% for the portside and starboard turning, and 40%, 51% for the torque coefficient in the experiment. The amount of decrease for the propeller efficiency is 47%, 53%. The overall errors for the propeller performance variables show a slight increase from the self-propulsion simulation by showing 5.9% and 6.7% averaged errors for the portside and starboard turning. The errors for the thrust coefficients during the two turnings are less than the error shown from the self-propulsion by being –3.6% and 4.3%. The difference between the two turnings is predicted similar to the experiment. However, the trend is the opposite. The errors for the torque coefficient are much less than the self-propulsion simulation by showing –0.5% and 2% errors for the portside and the starboard turning. Due to the over-prediction for the axial velocity and 4% errors for the propeller rotational speed (the error is little increased from the self-propulsion since the experiment used little larger value during the turning), the over-predicted advance ratio shows –15.6% and –16.7% errors for the portside and starboard turning. Still, the difference between the two turnings is almost similar between the experiment and the simulation.

The overall prediction accuracy for the self-propulsion factors for the starboard turning is similar to the accuracy found during self-propulsion simulation, while it shows about 10% larger averaged errors for the portside turning. Due to the inconsistent error shown from the propeller performance variables, the description for the error trend or the comparison with the self-propulsion are hard to be achieved. The open-water advance ratio is under-predicted with 19% error during the portside turning and over-predicted

with −7.9% error for the starboard turning. The error for the effective wake coefficient is under-predicted with 29% and 7.1% errors for both turnings. The error for the relative rotative efficiency is small by showing −0.3% and 3.3% for both turnings since the error for the torque coefficient is low. The errors for the propeller efficiency are 17.2% and −9.0% for both turnings.

The conclusions for the overall validation result are as follows: (1) the predicted errors for the portside turning is larger than the starboard turning with large difference for the IMO criteria, motions and self-propulsion factors, (2) affected from the sensitivity of the test condition, the errors increased for the secondly derived variables, i.e., self-propulsion factors, compared to the self-propulsion simulation, (3) the averaged error for the propeller performances is the lowest among the four different validation categories, which indicates the propeller performance is less sensitive to other validation variables during the turning, (4) the difference of variables between the portside and the starboard turning is mostly larger for the experiment, except for the self-propulsion factors implying the portside turning result is predicted less accurately from the simulation, (5) the large and distinct errors shown simultaneously for the axial velocity, roll angle, drift angle and the yaw rate from both turning indicates the strong correlation between the variables, (6) from the comparison of the trajectory shown in Fig. 11, the discrepancy of the trajectory for the portside turning occurs at the early stage of the turning (within $t^* = tU / L = 2$) affected by the axial/lateral velocity, the roll angle and the yaw rate indicating the balances of forces and moments are important during the transitional stage.

The local forces and moment balance during the steady-state turning are studied in the body-fixed frame using the same approach used for the self-propulsion simulation, and the result is shown in Table 12. To better understand the local forces and moment exerted on the bare-hull, the variables are undergone a further localization as shown in Fig. 14: the local forces and moment of the bare-hull are distributed on the 80 equidistance longitudinal stations. Compared to the self-propulsion simulation, the objective of the local forces and moments study more leans to identifying the most contributory assembly when deciding the axial/lateral velocity, drift angle, and yaw rate rather than identifying the factor causing the rudder angle as done from self-propulsion since the rudder is not active during the turning and the errors shown during the validation are much higher for the motions than the propeller performances, especially for the portside turning. Unlike the self-propulsion simulation, when the ship is in a steady-state circular motion during the turning, the axial and lateral force of the bare-hull, rudder and propeller become a role as a counterforce to be balanced with the centrifugal force. The equation of motion for the surge, sway, and yaw (Formulas (3), (4) and (8)) are simplified with the planar motion assumptions ($w \approx p \approx q \approx 0$) in steady-state, as presented in Formulas (27)-(29), which left the centrifugal forces at the LHS of Formulas (27) and (28).

$$-mvr = X_{\mathrm{BH}} + X_{\mathrm{RS}} + X_{\mathrm{MR}} + X_{\mathrm{PROP}} \tag{27}$$

$$mur = Y_{\mathrm{BH}} + Y_{\mathrm{RS}} + Y_{\mathrm{MR}} + Y_{\mathrm{PROP}} \tag{28}$$

$$0 = N_{\mathrm{BH}} + N_{\mathrm{RS}} + N_{\mathrm{MR}} + N_{\mathrm{PROP}} \tag{29}$$

In Table 12, the actual centrifugal force ($mr^2 R_T$) calculated with the yaw rate and the turning radius (R_T) in steady-state obtained from the experimental data are also presented to assess predicted counter-force which is balanced with the centrifugal force. Using the experimental data for the calculation of the actual centrifugal force instead of using the predicted values is due to the large validation errors shown from the IMO criteria and the motions, and thereby, the experiment value is considered more reliable.

The total axial forces exerted from the fluid are similar for both turning and are being used as the counterpart of the axial component of the centrifugal force. Comparing the axial force exerted to each assembly with the self-propulsion result, the resistance that the bare-hull experience decreases drastically due to the speed loss, the resistance for the moving rudder is 15 times larger due to rudder deflection and the propeller thrust is increased by 1.5 times due to operating at the low advance ratio condition.

Referring to Fig. 13, a large portion of the bare-hull resistance is reduced at the bow as the state of the ship becomes the circular motion. The rudder stock is the least contributory assembly for the total axial fluid force since the amount of force exerted on the rudder stock is very small. Since the validation errors shown for the propeller performance is low and the rudder force is rather considered subjective to the propeller performance, the dominant assembly deciding the total axial force, and resultantly deciding the axial velocity during the transitional stage, seems to be the bare-hull whose axial force is correlated with the drift angle. The axial component of the centrifugal force balance with the fluid exerted total axial forces with a very close amount explaining the constant axial velocity of the ship in the body-fixed frame. The total lateral force exerted from the fluid is nearly 3.3 times larger than the total axial force exerted from the fluid. The total lateral force shows a slightly larger value for

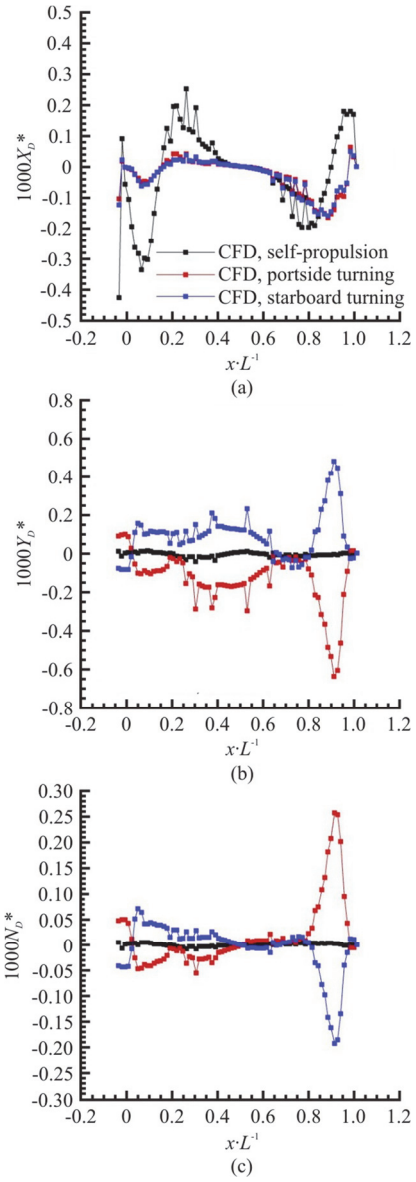

Fig. 14 (Color online) Longitudinal distributions of the hydrodynamic forces and moment acting on the bare-hull (SP and TC±35 simulations, steady-state, $g3$)

the starboard turning. However, the meaning of the difference is vague. Compared to the self-propulsion, the lateral force for both the bare-hull and the moving rudder increases significantly. Among all assemblies, the amount of the lateral force exerted to the bare-hull is the highest, with a large difference from the other assemblies. Once the lateral force of the bare-hull balances with the other assemblies, the residual force is balanced with the centrifugal force, which implies the bare-hull is the dominant assembly deciding the total fluid exerted lateral force as same as for the axial force. The distribution of the lateral force of the bare-hull is mostly biased to the negative side during the portside turning and vice versa, and the region that shows the largest lateral force is the stern when referring the Fig. 14. The lateral components of the centrifugal forces show close values to the fluid exerted lateral forces for both turnings. However, small discrepancies exist. The total yaw moment is close to zero, and the inertial force is not at present either. The yaw moment exerted to the bare-hull is no longer dominant, unlike the result shown from the lateral force balance. The large lateral forces shown from the bare-hull are mostly canceled out by being distributed with respect to the center of rotation with the same sign. The distribution of the yaw moment shows that most of the yaw moment is concentrated at the stern when referring to Fig. 14. The amount of the yaw moment exerted on the moving rudder is comparable to the yaw moment exerted on the bare-hull, and the rudder stock and the propeller are showing smaller yaw moments which amount to 10%-12%, 8%-10% of the yaw moment exerted to the moving rudder meaning that the effects from the rudder stock and the propeller are small. For the yaw moment, the moving rudder and the bare-hull are the dominant assemblies.

The conclusions on the local forces and moment study are like the followings: (1) the dominant assembly determining the axial velocity and the lateral velocity is the bare-hull and the forces exerted on the bare-hull is correlated with the drift angle, (2) the total

Table 12 Balances of local forces and moment and inertial force (TC±35 simulations, steady-state, $g3$)

Var.	TC-35					TC+35				
	BH	RS	MR	PROP	TOTAL	BH	RS	MR	PROP	TOTAL
$1000X^*$	–3.347	–0.167	–2.185	8.204	2.505	–3.618	–0.001	–1.903	8.011	2.489
$1000(-mvr)^*$	-	-	-	-	2.651	-	-	-	-	2.285
$1000Y^*$	–11.248	0.797	2.796	-0.407	–8.062	10.424	0.282	–2.513	0.150	8.342
$1000(mur)^*$					–8.953					7.227
$1000N^*$	1.571	–0.381	–1.358	0.195	0.027	–0.984	–0.134	1.214	–0.063	0.034
$1000(mr\sqrt{u^2+v^2})^*$	-	-	-	-	9.337	-	-	-	-	7.579
$1000(mr^2R_T)^*$(Exp.)	-	-	-	-	9.360	-	-	-	-	7.670

axial and lateral force exerted from the fluid, which are the residue after the balance, are being used as the counterforce to the centrifugal force whose amount is determined by the axial velocity, lateral velocity and the yaw rate. Therefore, the yaw rate is influential to the axial and the lateral force balance and the drift angle as well due to its strong involvement to the counterforce, (3) the yaw moment balance is not biased to the bare-hull unlike the balance shown for the axial and lateral force, and the amount of the yaw moment exerted on the bare-hull and the moving rudder are comparable which implies that deciding the yaw rate is more sensitive than deciding the axial and lateral velocities. In other words, the yaw rate and the yaw acceleration is highly viable with the change of the rudder angle, (4) the time history shows the earliest (within $t^* = 1$) abrupt increase for the yaw moment exerted on the moving rudder, which is the subjective response due to rudder deflection. The next earliest acceleration is shown for the yaw rate and the roll angle, which reach their maximum value at $t^* = 2$. The axial and lateral accelerations of the bare-hull, as shown from the time series of the axial and the lateral velocities, are much slower, which implies the importance of accurate prediction on the yaw acceleration during the early transitional stage for the accurate prediction of the trajectory, (5) Regardless of the transitional stage, the turning radius should be the same between the two specimens if the yaw rate, axial velocity and lateral velocity are the same during the steady-state, (6) during the steady-state turning where the roll angle and the drift angle are at present, the yaw moment exerted from the bare-hull is mostly concentrated at the stern where the pressure disturbance is induced by the bare-hull itself whose either side becomes similar as the suction side of the airfoil by being exposed to the incoming flow and experiences the larger axial speed than the other side, as shown in Fig. 15, which also explains the side force prevalent towards the inner side of the trajectory. Another factor for the pressure disturbance is the severe vortex which is generated as the transom touches the free-surface as shown in Fig. 16, however, the quantitative amount of effect is unknown, (7) in the lateral force balance, the non-negligible imbalance between the centrifugal force and the fluid exerted force is found which implies the imperfection of the simplified equation of motion due to the assumptions made for the derivation or possibly a flaw inside the code where the motions are integrated with the smoothed increment, (8) the total resultant centrifugal force, which is the root square sum of the axial and lateral components of the centrifugal force, shows distinct difference between the portside and the starboard turning and also follows the trend shown from the actual centrifugal force calculated with the experiment value even though the quantitative agreement between the two results is due to the over-prediction of the axial and lateral force and the under-prediction of the yaw rate.

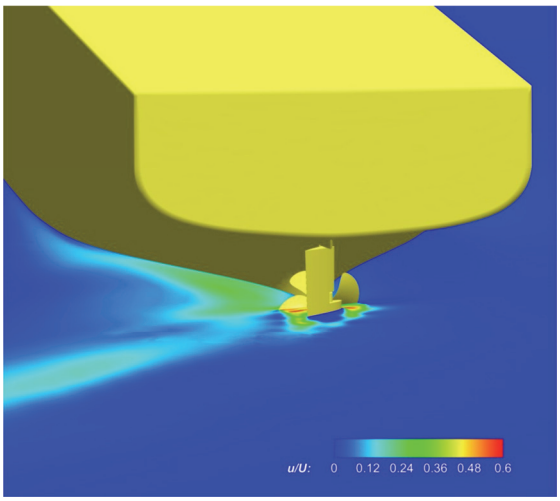

Fig. 15 (Color online) Axial velocity distribution on the lateral plane (TC-35 simulation, steady-state, $g3$)

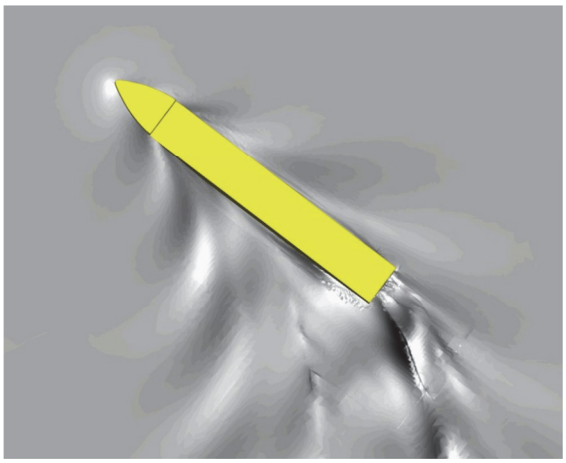

Fig. 16 (Color online) Free-surface distribution (TC-35 simulation, $g3$)

The correlation between the forces exerted on the single blade and the propeller inflow is found during the steady-state turning. An inference is made for the larger yaw moment exerted from the moving rudder during the portside turning. The approach is the same as the self-propulsion simulation. Figure 17 shows the mean propeller inflow during both turnings. Figure 18 shows the time series of the forces exerted from the single blade, and Fig. 19 presents the harmonic amplitudes of the axial force. The characteristics of the mean propeller inflow are like the following: (1) mean axial velocity is much less than the self-propulsion which induces a large amount of mean

thrust, (2) the distributions of the axial velocity of the propeller inflow from both turning shows much difference from the self-propulsion, however, the distributions are nearly symmetric, thereby, influencing the second harmonic of the thrust force, (3) the vortex patterns, which is found to affect the first harmonic of the thrust force during the self-propulsion simulation, are different over azimuthal angle for the turning as well, (4) the vortex pattern is not only different from the one shown from the self-propulsion, but also different between the portside and the starboard: the direction of the vortex shown from the portside turning is less favorable to the propeller rotation.

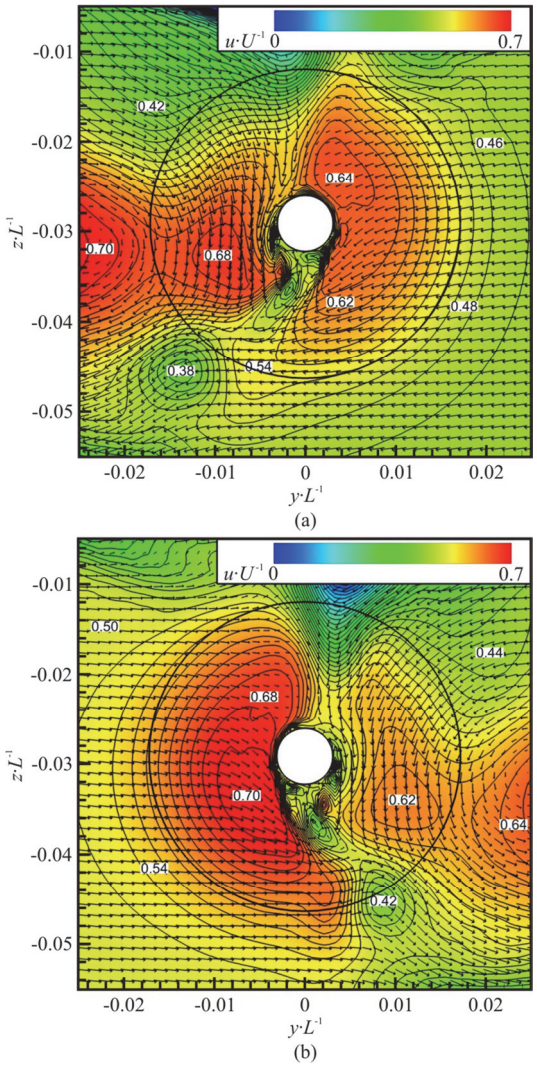

Fig. 17 (Color online) Mean propeller inflow (TC-35 (a) and TC+35 (b) simulations, steady-state, $g3$)

The characteristics of the propeller inflow are well reflected on the harmonic analysis performed for the forces of a single blade: (1) the mean value of the thrust is slightly larger for the portside turning which results in the larger mean rudder yaw moment as shown in Table 12, (2) the first harmonic amplitude of the thrust is larger for the portside turning due to the difference of the vortex pattern. The different vortex patterns between the two turnings have also affected the lateral and the vertical forces exerted on the blade, especially for the first harmonic amplitude of the vertical force, which will likely produce different propeller wake and affect the rudder differently, inducing different rudder force between two turnings.

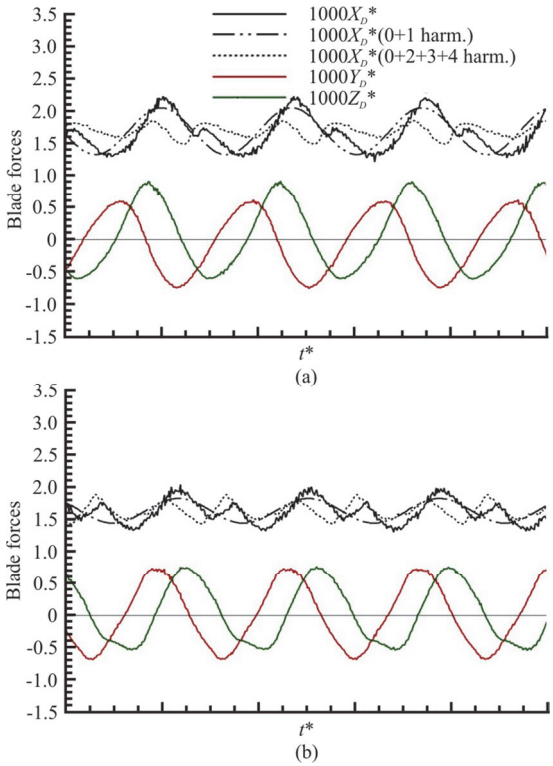

Fig. 18 (Color online) Time series of the hydrodynamic forces of a blade (TC-35 (a) and TC+35 (b) simulations, steady-state, $g3$)

5. Conclusions

In the propeller open-water simulation, the validation, and the grid study are performed for the propeller grid. The validation result confirmed the propeller grid shows the close propeller performances to the experiment data over a wide range of advance ratios. The grid study depends on the difference of solutions predicted with the grid triplet since the solution difference between the coarse and the medium grid is very small, and the convergence path often showed oscillatory behavior. The error for the torque coefficient is found to be almost doubled than the thrust coefficient. The error difference with respect to the grid resolution shows the same amount for the thrust coefficient and the torque coefficient

which implies the grid sensitivity is similar for both variables. The predicted thrust coefficients and the torque coefficients are fitted with the second polynomial and used for the thrust identification approach during the self-propulsion and the turning simulation.

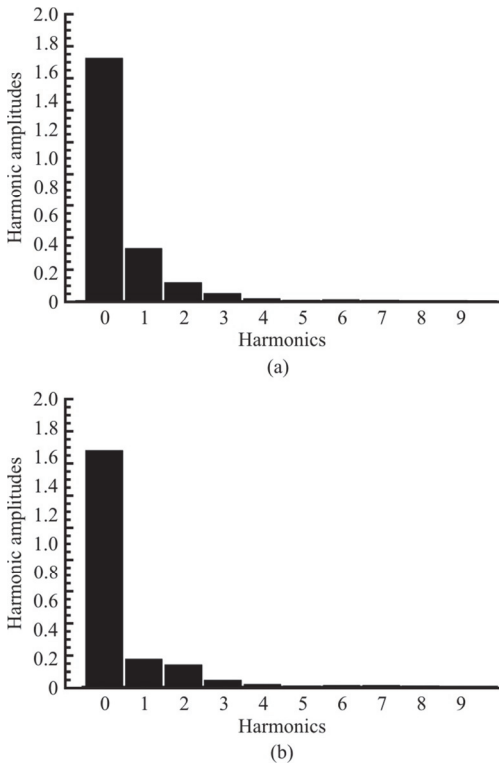

Fig. 19 Harmonic amp. of the hydrodynamic axial force of a blade (TC-35 (a) and TC+35 (b) simulations, steady-state, *g3*)

The resistance simulation validated the resistance components, sinkage, and trim for the bare-hull grid, and the grid study is performed. The errors shown from the validation study are in an acceptable range, and the grid study is affected by the motion oscillations, which is propagated from the abrupt speed change at the beginning of the simulation. However, the difference between the grid triplet is still found small. The mean propeller inflow at the inner side of the propeller perimeter extracted at the body-fixed frames shows the grid convergence, which ensures the accuracy of predicting propeller inflow for the turning simulations performed with the coarse grid.

The self-propulsion simulation is performed with the free-running condition. The validation and the grid study show satisfactory errors and small differences among the grid triplet for the motions and propeller performances. The errors for the self-propulsion factors are larger than the errors shown from the motions or the propeller performance, however, the prediction accuracy is still considered satisfactory. The local forces and moments study focus on describing the force and moment equilibrium at the course-keeping state and finding out the difference between the course-keeping and zero rudder angle conditions. The moving rudder is found to deflect and reach a neutral rudder angle condition favorable to the propeller wake and exert larger lateral force. The propeller wake, which influenced the moving rudder, is affected by the lateral and the vertical force exerted on the propeller blade and the lateral/vertical components of the surrounding wake induced from the bare-hull. The second harmonic thrust of a single blade is affected by the propeller inflow's symmetric axial velocity, and the first harmonic is prone to the vortex of the propeller inflow. The amount of the first and second harmonic amplitudes are comparable.

The IMO criteria and global variables are validated during the steady-state turning circle simulations. The overall error for the motion has increased while the variables for the propeller performance show similar or less errors compared to the result from self-propulsion simulation, implying the propeller performance is less sensitive to the chance of condition. The local forces and moments study focuses on finding out the dominant assembly for each equation of motion. The bare-hull is considered as the most dominant assembly determining the axial and lateral velocity, while the yaw is much sensitive than the others and prone to both the bare-hull and the moving rudder. The yaw moment from the bare-hull is mostly produced at the stern due to the flow characteristics near the bare-hull having the drift angle. The performance of a single blade correlated with the propeller inflow follows the same trend as shown from the self-propulsion and shows difference in the mean and the first harmonic of the thrust and the first harmonic of the vertical force due to experiencing different propeller inflow between the portside and starboard turning, consequently inducing larger rudder yaw moment for the portside turning.

Acknowledgement

This work was supported by the Office of Naval Research (Grant Nos. N00014-17-1-2083, N00014-17-1-2084).

References

[1] Sanada Y., Kim D., Sadat-Hosseini H. Experiment and numerical simulation for KCS added powering in regular head/oblique waves [C]. *32nd Symposium on Naval Hydrodynamics*, Hamburg, Germany, 2018.

[2] Sadat-Hosseini H., Wu P., Stern F. CFD simulations of KVLCC2 maneuvering with different propeller modeling

[C]. *Workshop on Verification and Validation of Ship Manoeuvring Simulation Methods*, Lyngby, Denmark, 2014.

[3] Sadat-Hosseini H., Stern F. 5415M maneuvering simulation using CFD free running and CFD-based SI [C]. *Workshop on Verification and Validation of Ship Manoeuvring Simulation Methods*, Lyngby, Denmark, 2014.

[4] Carrica P. M., Ismail F., Hyman M. et al. Turn and zigzag maneuvers of a surface combatant using a URANS approach with dynamic overset grids [J]. *Journal of Marine Science Technology*, 2013, 18: 166-181.

[5] Mofidi A., Carrica P. M. Simulations of zigzag maneuvers for a container ship with direct moving rudder and propeller [J]. *Computers and Fluids*, 2014, 96: 191-203.

[6] Muscari R., Dubbioso G., Viviani M. et al. Analysis of the asymmetric behavior of propeller-rudder system of twin screw ships by CFD [J]. *Ocean Engineering*, 2017, 143: 269-281.

[7] Zou L., Larsson L., Orych M. Verification and validation of CFD predictions for manoeuvring tanker [J]. *Journal of Hydrodynamics*, 2010, 22(5Suppl.): 438-445.

[8] Kaidi S., Smaoui H., Sergent P. Numerical estimation of bank-propeller-hull interaction effect on ship manoeuvring using CFD method [J]. *Journal of Hydrodynamics*, 2017, 29(1): 154-167.

[9] Wang J., Wan D. CFD study of ship stopping maneuver by overset grid technique [J]. *Ocean Engineering*, 2020, 197: 106895.

[10] Mentor F. R. Two-equation eddy-viscosity turbulence models for engineering applications [J]. *AIAA Journal*, 1994, 32(8): 1598-1605.

[11] Carrica P. M., Wilson R. V., Stern F. An unsteady single-phase level set method for viscous free surface flows [J]. *International Journal for Numerical Methods in Fluids*, 2007, 53(2): 229-256.